Aging-enhanced accumulation of fibroblasts excludes oligodendrocytes in demyelinated lesions

Brian M. Lozinski[1,], Charlotte D'Mello[1], Yifei Dong[1,2], George S. Melchor[3], Samira Ghorbani[1,4], Cenxiao Li[1], Marlene Morch[1], Dorsa Moezzi[1], Rajiv Jain[1], Parisa Etemadi[1], Chang-Chun Ling[5], Jeffrey K. Huang[3], Carlos Camara-Lemarroy[1], V. Wee Yong[1]*

[1]Department of Clinical Neurosciences and Hotchkiss Brain Institute, University of Calgary, Canada

[2]Department of Biochemistry, Microbiology and Immunology, University of Saskatchewan, Canada

[3]Department of Biology, Georgetown University, Washington DC, USA

[4]Department of Biology, University of Toronto Mississauga, Canada

[5]Department of Chemistry, University of Calgary, Canada

*Correspondence:

V. Wee Yong, PhD

Professor

University of Calgary

Calgary, Alberta T2N 4N1, Canada

vyong@ucalgary.ca

403-220-3544

Abstract

Fibroblast dysregulation contributes to aberrant repair and pathological fibrosis. Emerging evidence suggest that fibroblasts accumulate in lesions following central nervous system injury, but whether and how they influence oligodendrocytes and myeloid cell responses, especially in aging, is uncertain. Here we report that fibroblasts infiltrate the parenchyma of spinal cord white matter (SCWM) lesions after lysolecithin-induced demyelination. Transcriptomic analysis reveals diverse activation states of fibroblasts in lesions and communication networks between fibroblasts, microglia/macrophages and oligodendrocyte precursor cells (OPCs). The invasion of fibroblasts is facilitated by microglia/macrophages, and areas of fibroblast accumulation are devoid of OPCs. Fibroblast density is exacerbated with aging leading to greater fibrosis in lesions. Finally, we found fibroblasts in multiple sclerosis lesions with predicted communication networks between microglia/macrophages and OPCs. These results demonstrate a role of fibroblasts in demyelination-associated neuropathology, which is exacerbated by aging, and highlight the importance of regulating fibroblasts to promote effective CNS repair.

Introduction

Fibroblasts are a heterogeneous population of cells with important roles in extracellular matrix (ECM) synthesis, maintenance of cellular niches, tissue regeneration and wound healing[1]. To carry out their roles in homeostasis and injury fibroblasts form numerous interactions with other cell types including immune cells such as macrophages and T cells. Fibroblasts associated with the central nervous system (CNS) primarily reside in barriers including the meninges, perivascular space, and choroid plexus where they contribute to tissue homeostasis[2] and immune regulation[3,4]. Recent studies suggest that in response to injury, such as spinal cord trauma and experimental autoimmune encephalomyelitis (EAE), fibroblasts accumulate in the CNS parenchyma and contribute to fibrotic scaring[5–9]. This results from the ability of fibroblasts to respond to inflammatory and injury mediated signals promoting their activation. Activated fibroblasts differentiate into an ECM-producing smooth muscle actin (SMA)-expressing myofibroblast phenotype which can contribute either to tissue regeneration or fibrosis[10]. Thus, while fibroblast activation is necessary to maintain tissue integrity, it may also impair regenerative processes[5,11,12].

Remyelination is the most common and robust form of CNS regeneration[13]. Remyelination occurs when demyelination, such as that seen in multiple sclerosis (MS), stimulates the migration, proliferation, and differentiation of oligodendrocyte progenitor cells (OPCs) into mature myelinating oligodendrocytes[14]. Restoring myelin to denuded axons reconstitutes saltatory conduction, axonal trophic support, and produces a mechanical barrier to injury leading to axonal preservation and functional improvement[13,15,16]. However, remyelination often fails due to extrinsic variables in the environment, such as inhibitory ECM, and intrinsic factors including age-related cellular dysfunctions[16,17].

Age is a major contributor to disease worsening across a wide range of conditions, including MS and fibrotic disorders[18–20]. For example, fibroblasts in the skin and skeletal

68 muscles exhibit age-related dysregulation, characterized by altered lineage markers, increased
69 expression of inflammation-associated genes, and elevated ECM production[21–23]. In MS, OPCs
70 also show signs of age-related impairment, including upregulation of senescence markers,
71 epigenetic dysfunction, reduced responsiveness to growth factors, and impaired differentiation
72 and remyelination capacity[24–26]. While age-related remyelination decline is well recognized, the
73 impact of aging on fibroblast responses to CNS injury remains poorly understood.

74 In this study, we characterized the response of fibroblasts in lesions following focal
75 lysolecithin (LPC)-mediated demyelination of the spinal cord white matter (SCWM), and further
76 evaluated the influence of aging on the fibrotic response. With spatial transcriptomics of LPC
77 tissue and cells in culture, we interrogated interactions between fibroblasts,
78 microglia/macrophages and OPCs. Finally, we utilized a publicly available transcriptomic
79 dataset to show that fibroblasts are present in MS lesions, and describe communication patterns
80 between fibroblasts, microglia/macrophages and OPCs in MS. Our findings highlight the
81 necessity of considering invasion of fibroblasts into the CNS parenchyma in lesion evolution and
82 recovery.

83

Results

Fibroblasts are localized within demyelinated lesions

Although fibroblasts are restricted to CNS barriers in homeostasis, they are reported to be elevated in the parenchyma in models of traumatic spinal cord injury, stroke and autoimmune neuroinflammation[5,12,27]. While there is a growing appreciation for the functional connectivity of fibroblasts with other CNS resident cells, their roles in the regenerative processes of the CNS, primarily remyelination, remain poorly understood. The LPC model of demyelination provides an optimal system for studying neuroinflammation and remyelination due to the precise spatial location and temporal evolution of lesions[28,29]. LPC was stereotaxically injected into the ventral spinal cord white matter (SCWM) of mice resulting in a focal lesion characterized by damaged myelin (disrupted immunoreactivity for myelin basic protein, MBP), swollen axons as determined by neurofilament heavy chain staining (NFH), and GFAP-positive reactive astrocytes (Fig 1a). In PDGFRβTdTomato transgenic mice commonly used to study fibroblast responses in peripheral organs[30–32],we found TdTomato expression amongst the disrupted MBP-positive myelin debris and in close proximity to Iba1-positive microglia/macrophages (Fig 1b). As well, TdTomato and PDGFRβ immunofluorescence overlapped in LPC lesions giving confidence to the specificity of expression (Fig 1c). Further, we found that PDGFRβ was correspondent with a number of other markers of fibroblasts including collagen type 1 alpha 1 (Col1a1) and SMA for activated fibroblasts (Fig 1d).

We examined the fibroblast response at 7 and 21 days post injury (dpi) as periods when tissue regenerative responses begin to be robust and when they are concluding, respectively[17,28] (Fig 1e-j). While the total lesion volume was reduced from day 7 to 21 (Fig 1e, h), the total TdTomato-positive volume was comparable between 7 to 21 dpi (Fig 1f, i). Consequently, the proportion of the lesion occupied by fibroblasts was relatively greater at 21

compared to 7 dpi (Fig 1g, j). We then asked if fibroblasts differentiate into contractile ECM producing myofibroblasts using markers of ECM expression (fibronectin and periostin) and cell contractility (SMA) (Fig 1k). Approximately 40% of TdTomato-positive fibroblasts overlapped with these markers at 7 dpi (Fig 1l-n). In comparison, at day 21 TdTomato-labelled fibroblasts showed increased co-expression of SMA and periostin but decreased co-expression of fibronectin (Fig 1l-n).

We validated the fibroblast response in LPC lesions using single-nuclear RNA sequencing (snRNAseq) dataset at 5, 10, and 20 dpi (Fig 2a-c). Vascular and mesenchymal cells in LPC lesions were clustered and annotated into five groups: fibroblasts (*Col3a1, Col1a2, Col1a1, Bnc2, Dcn, and Foxp2),* endothelial cells (*Flt1, Pecam1, Ly6c1, Adgrl4),* pericytes (*Abcc9, Cspg4, Lin7a),* smooth muscle cell *(*SMC) *(Acta2, Myh11, Pdlim3, Lmod1),* and ependymal cells (*Adamts20, Cfap54, Dnah12, Agbl4, Cfap299)* (Fig 2a, b). *Pdgfrb* was expressed in fibroblasts, pericytes, and SMCs at variable levels (Fig 2a). We found that fibroblasts were significantly expanded in LPC lesions at all timepoints compared to naïve and non-lesioned samples (Fig 2b, c). Fibroblasts constituted ~75% of the vascular and mesenchymal cells 5 and 10 dpi, and approximately 60% at 20 dpi (Fig 2d). Further evaluation of the vascular and mesenchymal cell populations can be found elsewhere[33].

Collectively, our analysis of the fibroblast response to LPC injury using immunohistochemistry of the PDGFRβ-TdTomato reporter mice and snRNAseq of wildtype demyelinated mice confirms that activated fibroblasts expand rapidly and persist into late stages of LPC injury.

Spatial transcriptomics of fibroblasts in LPC lesions

To further investigate fibroblasts in the LPC lesion environment we used the 1000-plex Mouse Neuroscience Panel with the in-situ single cell CosMx spatial platform from Nanostring on three

sham and two LPC (14 dpi) lesioned spinal cords with 1 field of view (FOV) per section that demarcates the lesion area (Fig 3a, b). Day 14 LPC lesions were used as this is an intermediate period with ongoing remyelination[28,34]. We identified a total of 2954 segmented cells with (1828 cells from LPC and 1126 cells from sham controls). Unsupervised clustering of all cells revealed 12 clusters which were then mapped to the Azimuth mouse motor cortex reference map (Fig. 3c, d). This delineated the following cell types: astrocytes (*Gja1, Slc4a4, Slc6a1*), oligodendrocytes (*Mag, Mog, Myrf*), OPCs (*Pdgfra, Cspg5, Vcan*), microglia/macrophages (*Csf1r, Hexb, Csf3r*), vascular leptomeningeal cells (VLMCs) (*Dcn, Vtn, Igfbp7*), endothelial cells (*Cldn5, Pecam1, Flt1*) and pericytes (*Rgs5, Vtn, Myl9*) (Fig 3d, e). A separate identity was created for fibroblasts as cells which expressed *Col1a2* and *Pdgfrb* (Fig 3d, e). The UMAP in Fig. 3c shows an overlay of the clusters as coloured by cells from Sham and LPC mice. We identified a total of 84 *Col1a2* and *Pdgfrb* double-positive fibroblasts, 5 in sham controls and 79 in LPC lesions (Fig 3f, g). The top genes for fibroblasts aside from *Pdgfrb* and *Col1a2* were *Col3a1*, *Col1a1, Vtn* and *Dcn* (Fig 3e). The spatial analysis of LPC lesions affirmed that fibroblasts were 16 times more abundant in the parenchyma of LPC lesions at 14 dpi compared to sham (Fig 3g), and that fibroblasts were in close proximity to macrophages and OPCs (Fig 3b). Collectively, the spatial transcriptomic dataset shows an increased presence of fibroblasts in the injured CNS parenchyma during ongoing tissue regeneration and remyelination.

Fibroblast interactions in LPC lesions

We analyzed the spatial dataset for ligand-receptor (L-R) interactions and thus potential functions of fibroblasts within LPC lesions. Using the Cellchat package[35] we examined L-R interactions between fibroblasts, microglia/macrophages, and OPCs (Supplementary Fig 1a-d). We chose to investigate fibroblast interactions with OPCs as the latter are critical for remyelination, and with microglia/macrophages as they are the dominant immune cells in LPC lesions. Each interaction is assigned a probability value followed by a permutation test which

158 then allows us to make inferences about biologically significant cell-cell communication. Circle
159 plots and heatmaps delineated the aggregated cell-cell communication network between
160 fibroblasts, OPCs and macrophages in terms of number of interactions and total interaction
161 strength (Supplementary Fig 1a-d). Fibroblasts interacted most with OPCs, followed by
162 fibroblasts with themselves (Supplementary Fig 1a, c). In terms of total strength of interactions
163 this was determined to be highest between fibroblasts and microglia/macrophages
164 (Supplementary Fig 1b, d). Fibroblast derived ligands affected receptors involved in signaling
165 crucial for phagocytosis (*Pros1-Axl, Pros1-Mer*tk), macrophage polarization (*Spp1-Cd44, Apoe-*
166 *Trem2/Tyrobp*), cell adhesion (*Col1a1-Itgav/Itgb8*) and OPC survival (*Ptn-Ptprz1, Bdnf-Ntrk2*)
167 (Supplementary Fig 1f; Supplementary Fig 2a). Conversely, fibroblasts were predicted to
168 respond to L-R interactions that affect their survival, proliferation, differentiation, and migration
169 such as *Pdgfd-Pdgfrb*, *Fgf2-Fgfr2* and *Ptprs-Ntrk3* (Supplementary Fig 1g; Supplementary Fig
170 2b).

171 Predicted L-R interactions were also categorized into functionally related signaling
172 pathways. Fibroblasts were highlighted as the major driver of outgoing signaling in LPC lesions
173 among these three cell groups (Fig 4a; Supplementary Fig 1e). The signaling pathways that
174 contributed the most to outgoing fibroblast signaling included apolipoprotein E (APOE),
175 COLLAGEN, amyloid precursor protein (APP), prosaposin (PSAP) and FN1 (Fig 4a;
176 Supplementary Fig 3a). The outgoing microglia/macrophage signals were mainly contributed by
177 APOE, osteopontin (SPP1), colony stimulating factor (CSF) and GALANIN pathways. The
178 outgoing signaling from OPCs were mainly from pleiotrophin (PTN), Glutamate, neural cell
179 adhesion molecule (NCAM), and PDGF pathways (Fig 4a; Supplementary Fig 3a).
180 Microglia/macrophages were the primary recipient of L-R signaling through pathways such as
181 APOE, SPP1, and protein S (PROS) (Fig 4b; Supplementary Fig 3b). As well, OPCs responded
182 to COLLAGEN, PTN, and FN1 (Fig 4b; Supplementary Fig 3b). Although fibroblasts were not

identified as a dominant receiver of signaling through the cell types assessed they were inferred to receive signaling predominantly from COLLAGEN, GTPase-activating protein (GAP) and PDGF signaling pathways (Fig 4b; Supplementary Fig 1e).

To further contextualize the communication between fibroblasts, microglia/macrophages and OPCs, we utilized Cellchat's pattern recognition feature. This allows for the identification of global communication patterns to explore how the different cell groups and signaling pathways coordinate to function. This analysis uncovered three outgoing and three incoming signaling patterns that were dominated by individual cell groups (Fig 4c-f). The outgoing signaling from fibroblasts was characterized by pattern 1 which represented multiple pathways including COLLAGEN, vitronectin (VTN), and SPP1, while pattern 2 (which included signaling pathways such as endothelin (EDN), PTN, and VEGF) was driven by OPCs, and pattern 3 (which included signaling pathways such as leptin (LEP), GALININ, and CSF) by microglia/macrophages (Fig 4c, d). On the other hand, the communication pattern of target cells showed that incoming fibroblast signaling was dominated by pattern 3 which includes PDGF, nerve growth factor (NGF), and LEP pathways, while pattern 1 drove signaling (which included signaling pathways such as PTN, FN1, and EDN) in OPCs, and pattern 2 (which included signaling pathways such as APOE, APP, and CSF) drove signaling in microglia/macrophages (Fig 4e, f). Altogether this highlights the involvement of fibroblasts in the LPC environment as a major source of input for microglia/macrophages and OPCs.

Fibroblasts respond to microglia/macrophages

Since the spatial data analyses suggest that fibroblasts engaged in reciprocal communication with microglia/macrophages in the 14 dpi LPC lesion, we hypothesized that one cell type might help with the recruitment of the other into the area of injury. Indeed, Iba1+ microglia/macrophages and PDGFRβ+ fibroblasts were closely associated in day 7 LPC lesions (Fig 5). We thus examined 3 dpi and found that microglia/macrophages began accumulating in

the LPC lesion at day 3 before peaking at 7 days (Fig 5a-d). Similarly, the fibroblast response peaked at day 7 (Fig 5b, d). However, there was no observable PDGFRβ immunoreactivity at day 3 indicating that fibroblasts do not become elevated until after microglia/macrophage accumulation had begun (Fig 5a, d).

To corroborate the possibility that microglia/macrophages attract fibroblasts into LPC lesions, meningeal fibroblasts were added to the upper compartment of a Boyden chamber with bone marrow derived macrophages (BMDMs) or medium alone in the lower chamber (Fig 5e). After 24 hours there was a 3-fold increase in the number of fibroblasts that migrated across the membrane when cultured with BMDMs compared to the basal rate of migration (Fig 5f, g). These results suggest a role for macrophages in the promotion of fibroblast elevation in CNS lesions.

Fibroblasts spatially exclude OPCs

The CosMx Cellchat analyses suggest the interaction of fibroblasts with OPCs which we examined further. We found that at 14 dpi Olig2+ oligodendrocytes and Olig2+PDGFRα+ OPCs seemed to be restricted from regions of the LPC lesion that were occupied by PDGFRβ+ fibroblasts (Fig 6a). To determine whether this was previously surviving cells or newly responding OPCs, we utilized NG2CreER:MAPTmGFP mice that label newly differentiated oligodendrocytes with a membrane bound green fluorescent protein (GFP)[15,16]. Using this method, we found that areas within 14 dpi LPC lesions that were occupied by fibroblasts, based on PDGFRβ immunoreactivity, contained little GFP (Fig 6b, c). The difference in GFP was not due to axonal preservation as there was no difference in the density of NFH-positive axons in the fibroblast occupied region compared to the rest of the LPC lesion (Supplementary Fig. 4a, b). These results suggest that fibroblasts have the potential to regionally restrict OPC functions in LPC lesions.

To test this further we established cultures of meningeal fibroblasts in 96-well plates, upon which OPCs were then seeded (Fig 6d). No difference in total O4+ OPCs was observed when comparing OPC alone with those in co-cultured wells (Fig 6e). However, there was a significant decrease in the number of O4+MBP+ mature oligodendrocytes in co-cultured wells (Fig 6f). As well, oligodendrocytes in co-cultured wells displayed less complex morphological phenotypes than control cells grown without fibroblasts (Fig 6g). In controls, mature oligodendrocytes were able to spread in approximately even distribution around the cell soma (Fig 6d). In comparison, in co-culture, mature oligodendrocytes occupied only areas without fibroblasts and had more irregular orientations (Fig 6d). The restriction of mean outgrowth of oligodendrocytes by fibroblasts occurred regardless of the density of fibroblasts (Supplementary Fig 5a, b). As well, the inhibitory effect of fibroblasts was consistent regardless of the order that cells were seeded and was not recapitulated by culturing OPCs with fibroblast conditioned media (Supplementary Fig 5c, d). Collectively, this data highlights the inhibitory effect of fibroblasts on OPC differentiation.

Aging enhances fibroblast properties in LPC lesions

Age is a critical factor for many biological processes including tissue regeneration[36]. Aging is known to affect OPC and microglia/macrophage dynamics and is a critical factor in remyelination potential[17,18,37,38]. It is not known how the fibroblast response to CNS injury is affected by age and whether this impacts downstream processes. To test how age affects fibroblasts in LPC lesions, young (2-3 month) and middle-aged (12 month) mice were injected with LPC in the ventral SCWM. Tissue was collected 7, 14 and 21 dpi and immunostained for MBP and PDGFRβ (Fig 7a). Age did not affect lesion volume at 7 dpi but LPC lesions in middle-aged mice were significantly larger at 14 and 21 dpi (Fig 7b, d). Age also did not affect the PDGFRβ+ volume at 7 and 14 dpi, but did cause a significant increase at 21dpi in middle-aged

lesions (Fig 7c, e). When expressed in proportion to the lesion volume, the middle-aged LPC lesion has more fibroblasts than young LPC lesions at 7 and 21 dpi (Fig 7f).

We investigated the effect of age on the expression of phenotypic markers in fibroblasts in LPC lesions. Fibroblasts in day 7 LPC lesions in middle-aged demyelinated mice displayed elevated levels of activated myofibroblast marker SMA than those in their young counterparts (Fig 8a). While we did not find quantitative differences in Col1a1 or laminin at 7 dpi, these were elevated at 21 dpi (Fig 8b, c). Finally, we found significantly fewer Olig2+ oligodendrocyte lineage cells within the fibroblast-occupied regions of middle-aged compared to young mice (Fig 8d). Overall, we found elevated ECM levels in middle-aged mice that corresponded with a reduction in oligodendrocyte lineage cells in lysolecithin injury.

Fibroblasts are present in MS lesions

We extended from murine data into the human demyelinating condition, MS. Frozen brain sections from autopsied MS cases were stained for PDGFRβ as well as CD45 to identify leukocytes, and DAPI for cell nuclei (Fig 9a). We found that PDGFRβ+ cells were found in perivascular areas in close proximity to CD45+ leukocytes (Fig 9a).

Next, we reanalyzed previously published snRNAseq datasets from human brain tissues of MS lesion rim, core and periplaque; and white matter tissue from neurologically healthy controls[39]. Unsupervised clustering identified 25 clusters from the 66,432 total cells including leukocytes, Bergmann glia, dendritic cells, vascular endothelial cells, OPCs, oligodendrocytes, astrocytes, ependymal cells, microglia/macrophages, and neurons (Fig 9b). We highlighted a cluster of 174 cells that expressed fibroblast related genes[40] such as *PDGFRB*, *COL1A2*, *COL15A1*, *CEMIP*, *DCN*, and *FBLN1* (Fig 9c). From this cluster we focused on *PDGFRB*+ cells as our population of interest that were positive for the markers *PDGFRA*, *COL1A2*, *TGFBR3*, *FBLN1*, *DCN*, *COL15A1*, and *LAMC3* (Fig 9d; Supplementary Fig 6). Importantly, genes

associated with pericytes (*RGS5*), and smooth muscle cells (*TAGLN*) were not appreciably expressed in our population of interest (Supplementary Fig 7a)[41]. The *PDGFRB*+ fibroblasts were separated from the other cells in the dataset and re-clustered. This delineated 2 subpopulations (Fig 9e). Subcluster 1 expressed genes associated with stress response (*HSPB1*, *HMGB1*) while subcluster 0 expressed genes associated with ECM, cell proliferation, and migration (*LAMA2*, *NTRK3*) (Fig 9e; Supplementary Fig 7b, c). Assessment of these clusters via region showed that subcluster 0 was present in chronic active and chronic inactive edges and also the lesion core, but only minimally observed in control white matter or periplaque area; subcluster 1 was elevated only in the lesion core (Fig 9f).

Fibroblast interactions in MS lesions

We interrogated the interactions of fibroblasts with other cell types in MS lesions using CellChat L-R interaction analysis. Similar to LPC lesions, fibroblasts, microglia/macrophages and OPCs all communicated with each other (Supplementary Fig 8a-d). Fibroblast outgoing signals primarily involved ECM-receptor interactions while most incoming signals were via secreted signaling (Supplementary Fig 8e; Supplementary Fig 9 a, b). This is seen in the L-R pairings engaged by fibroblast derived ligands such as *COL1A2-ITGAV/ITGB9* and *LAMA2-CD44* (Supplementary Fig 8f; Supplementary Fig 9 a, b). As well, incoming secreted L-R interactions that fibroblasts were predicted to respond to included *FGF1-FGFR4* and *PDGFB-PDGFRA* (Supplementary Fig 8g; Supplementary Fig 9 a, b).

Fibroblast L-R pairs were further categorized into 76 signaling pathways such as transforming growth factor beta (TGFB), SPP1, PDGF, CSF, FN1, and COLLAGEN (Supplementary Fig 10a). Fibroblasts contributed to pathways that drove microglia/macrophage signaling including ephrin receptor A (EPHA), GAP, COLLAGEN, LAMININ, CSF, and CXC motif chemokine ligand (CXCL) (Figure 10a; Supplementary Fig 9c; Supplementary Fig 10a). Additionally, fibroblasts participated in signaling pathways that signaled at OPCs including bone

305 morphogenic protein (BMP), WNT, FGF, COLLAGEN, FN1, and LAMININ (Figure 10a;
306 Supplementary Fig 9c; Supplementary Fig 10a).

307 Communication patterns between cell populations highlighted three outgoing and three
308 incoming patterns (Fig 10a, b). Outgoing pattern one was primarily driven by OPCs. This pattern
309 was represented by pathways such as EPHA, VCAM, and NOTCH (Fig 10a). Pattern two was
310 driven mainly by microglia/macrophages defined by signaling pathways such as SPP1, PDGF,
311 and ANNEXIN (Fig 10a). The third outgoing pattern was defined primarily by fibroblast signaling.
312 This pattern was driven by pathways such as GAP, KIT, and plasminogen activator urokinase
313 (PLAU) pathways (Fig 10a). In the reverse, fibroblasts responded to incoming pattern three
314 represented by VCAM, neurotrophin (NT) and adhesion G protein-coupled receptor A2
315 (ADGRA) pathways (Fig 10b). OPCs responded to incoming pattern one that was driven by
316 signaling pathways including LAMININ, EDN, and WNT (Fig 10b). Microglia/macrophages
317 responded to pattern two that was defined by pathways including CSF, PLAU and TGFB (Fig
318 10b).

319 Comparison of the signaling pathways in LPC and MS lesions revealed 16.3% overlap of
320 outgoing fibroblast pathways and 15.3% of shared incoming pathways (Fig 10c, d). Shared
321 outgoing pathways included PDGF, PTN and COL1A1, and shared incoming pathways included
322 FGF, COL1A1 and VEGF (Fig 10c, d). Some unique fibroblast signaling pathways in MS
323 included outgoing PLAU and TGFB signaling and incoming WNT and TGFB signaling (Fig 10c,
324 d). Within these pathways we identified that there were 16 conserved outgoing fibroblast L-R
325 interactions and 10 conserved incoming fibroblast L-R interactions; these include fibroblast
326 derived FGF1 and PTN signaling to FGFR2 and PTPRZ1 respectively and, fibroblast CD44 and
327 NTRK3 responding to COL1A1 and PTPRS respectively (Supplementary Fig 10c, d). There
328 were similarities in the L-R interactions of fibroblasts in MS and LPC lesions such as outgoing L-
329 R interactions (*PROS1-MERTK*, *PTN-PTPRZ1*, *FGF1-FGFR2*, and *COL1A1-CD44*), and

incoming interactions (*FGF2-FGFR2*, *PTPRS-NTRK3*, *COL1A1-ITGAV/ITGB8*, and *COL4A5-CD44)* (Fig 10c, d; Supplementary Fig 2; Supplementary Fig 3; Supplementary Fig 9a, b; Supplementary Fig 10c, d).

Overall, it appears that microglia/macrophages and OPCs employ multiple signaling pathways compared to fibroblasts. Furthermore, cross-referencing the outgoing and incoming patterns highlighted that some pathways such as VCAM are shared by all three cell groups assessed with microglia/macrophages and OPCs both contributing to outgoing VCAM signaling and fibroblasts as sole responder (Supplementary Fig 10a, b). Taken together these data highlight not only the presence of fibroblasts in MS lesions but also their prominent interactions with microglia/macrophages and OPCs in their environment.

Discussion

The accumulation of fibroblasts in the parenchyma of CNS lesions has received scant attention due to the lack of a prominent marker that clearly distinguishes this cell population, and because antigens that label them (e.g. PDGFRβ, NG2 or GLAST) are also present on other cell types such as pericytes and smooth muscle cells[4]. Nonetheless, combining markers such as PDGFRβ and Col1a1 has elevated confidence in detecting fibroblasts and an increasing literature now implicate them in models of traumatic CNS injury and MS[5,7–9,12]. Previously, PDGFRβ positive cells were described in the core of the scar resulting from traumatic spinal cord injury[12,42] although their cellular identity (e.g. fibroblasts or pericytes) could not be definitively discerned. Additional recent reports describe perivascular fibroblasts with angiogenic and fibrogenic functions[43]. In the current study, the presence of fibroblasts using a PDGFRβ-TdTomato reporter[30,31,44] and additional staining markers (Col1a1, SMA, fibronectin, periostin) affirm the presence of fibroblasts in the parenchyma of CNS lesions of LPC injury and MS. Highly

354 multiplexed RNA in situ hybridization (RNA-ISH, CosMx), which revealed additional fibroblast
355 transcriptome (*Col1a2, Col3a1, Vtn, Dcn, Cfh* and *Fbn1*), showed that there was a 16-fold
356 increase in fibroblasts in the LPC lesion compared to sham controls. Moreover, the absence of
357 *Rgs5*, a commonly used pericyte marker, lend further support to the identification of fibroblasts.
358 In the LPC model, fibroblasts are present in day 7 lesions, a period when the repopulation of
359 OPCs is at its peak and remyelination is beginning[28,34]. The period between day 7 and day 21 is
360 when OPCs differentiate and remyelination proceeds progressively albeit incomplete[17,34]. We
361 find that fibroblasts persist in the LPC lesion from 7 to 21 days with no resolution.

362 The accumulation of fibroblasts in LPC injury appears to be facilitated by
363 microglia/macrophages as suggested by the temporal relationship where fibroblasts do not
364 become elevated until after onset of neuroinflammation, and the in vitro results that show
365 macrophages to be chemotactic for fibroblasts. Transcriptomic data with Cellchat analyses
366 suggest microglia/macrophages and fibroblasts communicate through numerous signaling
367 pathways/molecules including PDGF which is a known chemotactic signal for fibroblasts[45].
368 Indeed, macrophage-derived PDGF has been proposed as one half of a reciprocal cell-circuit
369 with fibroblast derived M-CSF that is critical for regulating tissue fibroblast responses[46,47].
370 Further studies will be required to determine the predominant microglia/macrophage-derived
371 signals that promote accumulation of fibroblasts in LPC lesions.

372 Fibroblasts have been reported to be inhibitors of axon regrowth[11]. However, little is
373 known about the potential effect of fibroblast accumulation on the most common form of CNS
374 regeneration, remyelination. Analysis of L-R interactions predicted from our CosMx dataset
375 suggests that fibroblasts are a potent driver of signaling in LPC demyelination. Importantly for
376 remyelination, we found that the many of the fibroblast-derived ligands that can affect OPCs are
377 ECM genes including *Fn1* and *Col1a1*[43]. Accumulation of inhibitory ECM components impair
378 OPC function and reduce remyelination[16,48]. Aside from its role as a structural protein,

379 fibronectin can form aggregates that impair OPC maturation[49]. The effect of collagens on OPC
380 functions are less understood, although impaired migration may occur[5]. ECM components can
381 also impede OPC function through indirect effects including by stimulating
382 microglia/macrophages and lymphocytes that kill OPCs[49]. Furthermore, how potential fibroblast-
383 led signaling interactions continue to influence remyelination requires further investigation, as
384 fibroblasts are transcriptionally dynamic throughout remyelination[33].

385 It is also possible that fibroblasts provide a physical obstacle to oligodendrocyte
386 processes that are contacting axons for remyelination. This is supported by our in vivo results
387 that regions of an LPC lesion occupied by fibroblasts have few OPCs or newly formed myelin
388 compared to the unoccupied areas of LPC lesions. Furthermore, in vitro co-culture of fibroblasts
389 with OPCs show a density dependent curve of fibroblast inhibition. Additional experiments
390 focusing on the depletion or reduction of fibroblasts within LPC lesions will provide clarity to the
391 mechanisms regulating the inhibition of oligodendrocyte lineage cells by fibroblasts.

392 We did attempt to deplete fibroblasts using PDGFRβCre:Rosa26iDTR mice but these
393 cells remained persistent in lesions (data not shown). In a report in EAE, reducing fibroblast
394 proliferation by fibroblast-specific expression of the herpes simplex virus thymidine kinase gene
395 produced a modest improvement in clinical disability and an elevation of oligodendrocyte
396 lineage cells[5].

397 Age is a major contributor to overall morbidity and the reduced efficiency of many
398 biological processes[36] including the formation of oligodendrocytes[50] and remyelination[17,51]. We
399 found a greater number of fibroblasts in LPC lesions of middle-aged compared to young mice.
400 While there is a reduced rate of accumulation of microglia/macrophages within lesions of aging
401 compared to young mice, these cells in aging animals in 'inflammaging' are more capable of
402 producing inflammatory cytokines, chemokines and other molecules[52,53]. Indeed, a greater
403 number of mononuclear phagocytes in aging CNS lesions are positive for *Spp1* which encodes

404 for the glycoprotein osteopontin[18]. *Spp1* positive macrophages have been shown to drive the
405 activation of myofibroblasts leading to increased tissue fibrosis[54]. We found in both our CosMx
406 dataset and in the reanalysis of MS snRNAseq data that *Spp1*-positive microglia/macrophages
407 are present in both LPC and MS lesions. Thus, the increased presence of fibroblasts in middle-
408 aged LPC lesions may contribute to worse remyelination outcomes noted with aging as we find
409 that there are fewer oligodendrocyte lineage cells in fibroblast occupied regions. As well,
410 fibroblasts in lesions of middle-aged relative to young mice express greater amounts of ECM
411 components which may contribute to already existing OPC dysregulation.

412 To extend from animal models to MS, we stained and identified PDGFRβ positive cells in
413 close proximity to CD45 positive leukocytes. We next analysed a single-nucleus RNA
414 sequencing dataset of MS[39] and found a small population of presumptive fibroblasts; it is
415 possible that the cell isolation process was not optimized for fibroblasts and thus did not
416 adequately capture the entirety of the number of these cells in lesions. Nonetheless, we
417 identified a population of *PDGFRβ* positive cells that expressed genes associated with
418 fibroblasts, and similar to those found in LPC lesions, such as *COL1A2, COL15A1, DCN and*
419 *FBLN1*. It is noteworthy that these cells are found in lesions but minimally in the periplaque area
420 or neurologically normal white matter, indicating their association with pathology in MS. As with
421 LPC injury, the Cellchat analyses of MS brain cells indicate the immense potential of fibroblasts
422 to interact with microglia/macrophages and oligodendrocyte lineage cells.

423 Fibroblasts have been identified in a number of neurological disorders such as
424 Alzheimer's Disease and stroke[4,40]. By using multiple markers simultaneously, it is likely that
425 fibroblasts will be detected in the parenchyma of the CNS of most neurological conditions. While
426 their numbers in the CNS parenchyma do not appear high (an estimated 5-10% on LPC lesions
427 by spatial transcriptomics), their potent capacity to exclude oligodendrocytes from lesions and

their many potential interactions with microglia/macrophages and CNS cells position them to be important regulators of pathophysiology and recovery.

In conclusion, we provide evidence that fibroblasts accumulate in the parenchyma of demyelinated lesions including in MS. We show that fibroblast-occupied areas lack new myelinating cells, and that fibroblasts inhibit OPC differentiation in vitro. Importantly, this process is exacerbated by age leading to greater fibrosis of the lesion. These results highlight the necessity of targeting fibroblasts to mediate regenerative processes and improve outcomes in neurological conditions.

Acknowledgments

We acknowledge operating grant support from MS Canada, USA Department of Defense Multiple Sclerosis Research Program, and the Canadian Institutes of Health Research (CIHR). BML and DM received PhD studentship awards, and RJ a postdoctoral fellowship, from MS Canada. YD and SG were recipients of postdoctoral awards from CIHR. MM received a postdoctoral fellowship from Lundbeck Foundation, Denmark.

Contributions of authors

BML conducted the majority of the experiments and acquired and analysed the results; he wrote the initial drafts of the manuscript. CDM contributed bioinformatics and transcriptomic expertise, and led the acquisition of home grown or public domain transcriptomic results. YD, GSM, SG, CL, MM, DM, and RJ provided tissue samples for the manuscript; GSM also provided single-nucleus RNA sequencing results and figure panels. PE contributed to datasets of the aging experiments. CCL (Ling) contributed expertise in chemistry of the extracellular matrix. JKH

contributed datasets of single-nucleus RNA sequencing in lysolecithin-demyelinated mice. CCL (Camara-Lemarroy) contributed datasets of spatial transcriptomics of lysolecithin lesions. All authors edited and approved the manuscript. VWY oversaw the entire project including the acquisition of funds and finalizing the manuscript.

Competing interests

The authors declare no conflict of interest.

Materials and Methods

MS specimens

Postmortem frozen brain tissues from people with MS were obtained from The Multiple Sclerosis and Parkinson's Tissue Bank situated at Imperial College, London (https://www.imperial.ac.uk/ medicine/multiple-sclerosis-and-parkinsons-tissue-bank). All samples at their local sites were collected with full informed consent for autopsy. Human tissue use in Calgary for research was approved by the Conjoint Health Research Ethics Board at the University of Calgary (Ethics ID REB15-0444). MS sections were characterized using luxol fast blue (LFB) and hematoxylin & eosin (H&E) to identify lesions as previously described[55].

Mice

All experiments were conducted with ethics approval from the Animal Care Committee at the University of Calgary under regulations of the Canadian Council of Animal Care. Female C57BL/6J mice were from Jackson laboratories. CX3CR1-CreER (JAX 021160), iDTR [Rosa26^{iDTR} (JAX 007900)], PDGFRβ-P2A-CreERT2 (JAX 030201), Ai9 [Rosa26-TdTomato (JAX 007905)], NG2-CreER (JAX 008538), and Tau-mGFP (JAX 021162) mice were from The Jackson Laboratory. PDGFRβ-P2A-CreERT2, Ai9 [Rosa26-TdTomato] mice were bred in the single barrier mouse unit at the University of Calgary to produce female PDGFRβ^{TdTom} mice for

fate mapping experiments. NG2-CreER and Tau(Mapt)-mGFP mice were bred in the single barrier mouse unit at the University of Calgary to produce female NG2-Mapt^{mGFP} mice for OPC maturation experiments. All young female mice were 6-10 weeks of age, and all middle-aged female mice were 48-52 weeks of age. Male and female CD1 pups P0-2 were used for OPC and meningeal fibroblast cultures. C57BL6 female mice 6-10 weeks of age were used for bone marrow-derived macrophages (BMDM) cultures. All mice were maintained on a 12-h light/dark cycle with food (Pico-Vac Mouse Diet 20) and water given ad libitum.

Spinal cord surgery

Lysolecithin/lysophosphatidylcholine (LPC) demyelination was accomplished as previously described[56]. Mice were anaesthetized with intraperitoneal injections of ketamine (100 mgkg-1) and xylazine (10 mgkg-1). Buprenorphine (0.05 mgkg-1) was given as an analgesic. The surgery site was shaved and disinfected with 70% ethanol and betadine. Mice were positioned on a stereotaxic frame and a 2-3 cm incision was made between the shoulder blades. The intervertebral space between T3 and T4 was identified, blunt dissected apart, and the exposed dura was removed using a 30-gauge metal needle. Using a 32-gauge needle attached to a 10 µL Hamilton syringe, 0.5 µL of 1% w/v LPC (Sigma-Aldrich, L1381) was injected into the ventral column of the spinal cord at a rate of 0.25 µLmin-1 for 2 min. The needle was left for 2 min following the injection to avoid back flow. Muscle and skin were then sutured, and mice placed in a thermally controlled environment for recovery.

Spinal cord tissue isolation

LPC mice were anaesthetized as described above. Mice were then transcardially perfused with 15 mL of PBS. Spinal cords were removed drop fixed in 4% paraformaldehyde (PFA) at 4°C overnight. Tissue was cryoprotected in 30% w/v sucrose solution for 72-hours then frozen in

FSC 22 frozen section media (Leica). Coronal sections were generated with a cryostat (ThermoFisher Scientific) onto Superfrost Plus microscope slides (VWR) and stored at -20°C until analysis.

Immunofluorescence staining

Slides were thawed for 10 minutes, rehydrated for 10 minutes with PBS, and permeabilized with 0.2% TritonX-100 in PBS for 10 minutes. Tissue was blocked for 1 hour at RT with horse serum blocking solution (0.01 M PBS, 10% horse serum, 1% bovine serum albumin (BSA), 0.1% cold fish skin gelatin, 0.1% Triton-X100, and 0.05% Tween-20). Primary staining was done overnight at RT in buffer (PBS, 1% BSA, 0.1% cold fish stain gelation, 0.1% Triton X-100). Slides were washed 2 x 5 minutes with PBS, and stained with TrueBlack Lipofuscin Autofluorescence Quencher (Biotium) for 2 min at room temperature. Slides were washed 3 x 5 minutes, then incubated with secondary antibodies and 1 μgmL-1 of DAPI resuspended in buffer for 1 hour at RT. Slides were washed 3 x 5 minutes, and mounted with Fluoromount-G solution (SouthernBiotech). Antibodies used: anti-mouse myelin basic protein (MBP, BioLegend, PA1-10008), anti-mouse POSTN (R&D Systems, AF2955), anti-mouse αSMA-Cy3 (Millipore, C6198), anti-mouse FN1 (Millipore, AB2033), anti-CD45 (Thermofisher, MA5-17687), rabbit anti-mouse pan-laminin antibody (a gift from L. Sorokin, University of Münster, Münster, Germany; 1:1000), anti-mouse/human PDGFRβ (R&D Systems, AF1042), anti-mouse Iba1 (Wako, 019-19741), anti-mouse CD45-AF488 (Biolegend, 103122), Col1a1 (Invitrogen, PA1-26204), anti-mouse GFAP (Biolegend, PCK-591P), anti-mouse NFH (RPCA-NF-H), anti-mouse PDGFRα (R&D Systems, AF1062), anti-mouse Olig2 (Millipore, ab9610), GFP (Aveslab, GFP-1020), anti-mouse sulfatide O4 (R&D Systems, MAB1326), anti-mouse Arg1 (BioLegend, 678802), and anti-mouse MHCII (Thermofisher, 13-5321-82). Secondary antibodies from Jackson ImmunoResearch were used at 1:400 dilution: AF488 donkey anti-mouse IgM, AF488 donkey anti-rabbit IgG, AF488 donkey anti-rat IgG, AF488 donkey anti-goat IgG, cyanine Cy3

donkey anti-goat IgG, cyanine Cy3 donkey anti-chicken IgY, AF647 donkey anti-rat IgG, and AF647 donkey anti-rabbit IgG.

Confocal immunofluorescence microscopy

Images were acquired on a Leica TCS Sp8 laser confocal microscope or Leica Sp8 Falcon. Leica TCS images were taken using a ×25/0.5 NA water objective. The 405-nm, 488-nm, 552-nm and 640-nm lasers were used and detected by two low-dark-current Hamamatsu PMT detectors and two high-sensitivity hybrid detectors. Leica SP8 Falcon images were taken using a x20/0.8 NA air objective with 405nm and white light laser (470-670nm), and detected by one low-dark-current Hamamatsu PMT detector, one cooled high sensitivity, single molecule detection hybrid detector, and two high sensitivity hybrid detectors. All images were acquired using the following parameters: in 8 bits, in a z-stack using unidirectional scanning, 1 times frame averaging, 1 airy unit pinhole, ×1 zoom, 0.57 µm or 1 µm per optical section, and 2,048 x 2,048 or 1024 x 1024 pixels x–y resolution. Equal laser, gain and offset settings to maximize contrast and minimize saturation were consistently used for all samples within each set of experiments. All lesions were imaged for volume measurements and sections at the lesion epicenter were used for all other analysis.

Cell culture

Mouse meningeal fibroblasts

Meninges from P0-2 CD1 pups were collected in RPMI and digested for 18 minutes at 37°C in 1 µgmL-1 DNase I (Sigma) and 3.7 µgmL-1 collagenase D (Sigma) triturating every 6 minutes. Meninges were centrifuged at 300xg for 3 minutes and cells were resuspended in growth medium (DMEM (Gibco) supplemented with 10% FBS, 1% non-essential amino-acids (NEAA), 1% GlutaMAX, 1% sodium pyruvate, and 1% penicillin-streptomycin (all from Gibco). Cells were

548 incubated in T-75 flasks at 37°C with 5% CO2. Medium replaced every 3 days and cells were
549 passaged when 90% confluent. Cells were used after at least one passage.

550 *Mouse oligodendrocyte progenitor cells (OPCs)*

551 Mouse OPCs were cultured as previously described[16]. Briefly, cortices from P0 CD1 pups were
552 removed and dissociated with papain (Worthington), DNase (Sigma), and L-cysteine (Sigma) for
553 30 minutes at 37°C. Cells were cultured in mixed glial culture growth medium in poly-L-lysine
554 coated T-75 culture flasks. Medium changes were performed 3–4 h, and days 3 and 6.
555 Supplemented medium was added from day 6. On day 9, flasks were shaken for 45 minutes
556 and medium replaced with 10-12mL of insulin supplemented mixed glial culture medium. Flasks
557 were shaken at overnight at 37°C, 5% CO2 and the supernatant was transferred to a 100 mm
558 tissue culture dish for incubation at 37°C and 5% CO2 for 30 min with gentle swirling by hand
559 after 15 minutes. OPC enriched medium was collected, centrifuged at 300xg for 10 min, and
560 seeded at 3,200 cells/cm^2 density in oligodendrocyte differentiating medium. Plates were left at
561 37°C and 8.5% CO2 for 24–72 h. 96-well flat bottom black/clear plates pre-coated with poly-L-
562 lysine was used.

563 *Mouse bone marrow-derived macrophages (BMDMs)*

564 Cells were collected by flushing femurs with DMEM supplemented with 10% FBS, 1% penicillin-
565 streptomycin and 1% glutamax (all Gibco). Cells were centrifuged at 300xg x 10 minutes,
566 supernatant was discarded, and cells resuspended in BMDM culture medium (10% supernatant
567 from L929 cell line enriched in macrophage-colony stimulating factor, 10% FBS, 1% penicillin-
568 streptomycin, 2% minimum essential medium MEM non-essential amino acid solution (all
569 except L929 from Gibco). Cells were cultured in 100 mm culture plates at 37°C with 8.5% CO2
570 for 9 days. Medium was half changed day 5 and full changed day 9. Day 9, BMDMs were

collected using cold PBS and scraping cells. Cells were collected into 50 mL tubes, spun at 300xg for 10 minutes, and resuspended in 1 mL of BMDM culture medium for counting.

Cocultures

OPCs were added at a density of 31,250 cells/cm^2 to poly-L-lysine coated 96-well plates. Meningeal fibroblasts were added at densities of 31.25, 312.5, 3125, 31250, 312500, and 10000 cells/cm^2 as listed. OPCs and meningeal fibroblasts were added together, or one added 2 hours before the other as defined in the experiment, in 100 µL of OPC differentiating medium. Cocultures were incubated at 37°C with 8.5% CO_2 for 72 hours. Cells were fixed with 4% PFA for 10 minutes then stored in PBS until staining. Tissue was blocked with Licor Blocking Buffer for 1 hour at RT. Anti-O4 primary antibody was added in Licor antibody dilution buffer (1:250) overnight at 4°C. Cells were washed 3 x 5 minutes with PBS then donkey anti-mouse IgM AF488 secondary antibodies were added (1:200) for 1 hour at RT. Cells were washed 3 x 5 minutes each in PBS and permeabilized for 5 minutes with 0.02% Triton-X100 in PBS. Cells were washed once with Licor blocking buffer, then incubated overnight at 4°C with anti-PDGFRβ (1:50; R&D systems;AF1042) and anti-MBP (1:100; Abcam; ab7349). Cells were washed in PBS-Tween 0.1% and stained with secondary antibodies (1:200) for 1 hour at RT on a shaker. Cells were washed 3 x 5 minutes each and suspended in PBS with 1 μg/mL DAPI. Plates were kept covered at 4°C until imaged.

Transwell migration assay

BMDMs were plated in 24 well plates at a density of 260,000 cells/cm2 overnight at 37°C with 8.5% CO2. Medium with 1% FBS was added for 24 hours prior to experiments. Meningeal fibroblasts (150,000 cells/cm2) were added to transwell inserts (Corning, 29442-120) for 16-18 hours, then fixed and stained. The upper chamber was cleaned using a cotton swab, inserts were fixed with acid alcohol (1% HCl in 95% ethanol) for 15 minutes then washed in PBS for 5

minutes. Inserts were transferred to hematoxylin for 15 minutes, and washed in PBS for 1 minutes. Inserts were mounted and imaged on an Olympus VS110 slide scanner on a 10x/0.4 NA objective and VS-ASW-S5 (V2.9) with Batch Converter software.

Fluorescent image analysis

Leica Application Suite X was used for image acquisition, ImageJ for image threshold and particle analysis, and QuPath 0.3.1 for transwell and slide scanner image analysis. Maximum-intensity projections were created for each channel/marker. All images were blinded prior to analysis. ROI for lesions were drawn using DAPI or MBP. Fibroblast regions were defined using PDGFRβ. Threshold intensity was determined using at least 3 images. The Analyze Particles function was then used to create a mask and to quantify the positive signals in each ROI using size exclusion of 2-infinity. Threshold intensity, size exclusion, and circularity settings for particle analysis were kept constant across all samples for each experimental set. Oligodendrocytes were counted manually using Olig2 and DAPI as a guide. When analyzing lesion spread samples were excluded if more than 20% of sections were unable to be analyzed due to tearing, folding, or other loss.

Quantitative fluorescence microscopy analysis

Plates were imaged using a ×10/0.5 NA air objective on an ImageXpress Micro XLS High-Content Analysis system (Molecular Devices). The following filters were used for detection: DAPI, excitation of 387/11 and emission of 447/60; FITC, excitation of 482/35 and emission of 536/40; Cy3, excitation of 531/40 and emission of 593/40; and Cy5, excitation of 628/40 and emission of 692/40. For quantification, 9–12 FOVs were imaged per well. Multiwavelength cell scoring analysis in the MetaXpress High-Content Image Acquisition and Analysis software (Molecular Devices) was used to quantify cell survival from the fluorescence microscopy images gathered. For fold change values, all numbers were divided by the mean of the control samples.

The fold-change values from all samples and experiments were then plotted for statistical analysis. For the representative images shown, each channel/marker for the sample was merged and displayed using pseudocolours.

CosMx spatial molecular imaging

Slides with FFPE sections as prepared above were sent to NanoString for analysis using the CosMx platform. Sample processing, staining, imaging, and cell segmentation were performed as previously described[57]. The 1000-plex CosMx Mouse Neuro probe panel was used along with markers for morphology and cell segmentation: GFAP, Histone_H3, 18S- rRNA and DAPI. A 0.51mm FOV was centered on the lesion area. The CosMx optical system has an epifluorescent configuration based on a customized water objective (13×, NA 0.82), and uses widefield illumination, with a mix of lasers and light-emitting diodes (385 nm, 488 nm, 530 nm, 590 nm, 647 nm) that allow imaging of DAPI, Alexa Fluor-488, Atto-532, Dyomics Dy-605 and Alexa Fluor-647, as well as removal of photocleavable dye components. Nine Z-stack images (0.8 um step size) of each FOV were acquired and then fluorophores on the reporter probes were UV cleaved and washed off with Strip Wash buffer. This procedure was repeated for the remaining 15 reporter pools, and the 16 cycles of reporter hybridization-imaging was repeated 8 times to increase RNA detection sensitivity. Raw image processing and feature extraction were performed using an in-house SMI data processing pipeline which includes registration, feature detection, and localization[57]. A cell segmentation pipeline using machine learning algorithm was used to accurately assign transcripts to cell locations and subcellular compartments as previously described[58].

CosMx data processing

Data from the CosMx platform was formulated into an object for Seurat v5 package [59] in R programming environment. Data from 2 LPC and 3 Sham brain sections with FOVs from the

right hemisphere were used. Data was normalized using SCTransform v2. An unsupervised analysis and generation of a final UMAP with 20 PCs and resolution = 0.7 was done. The package Harmony [60] was used to integrate 'Group' data (group.by.vars = group (LPS or Sham). Robust Cell Type Decomposition (RCTD) was used to map the cluster profiles to the Azimuth mouse motor cortex reference map (azimuth.hubmapconsortium.org). The following cell types were identified: astrocytes, endothelial cells, neurons, macrophages, oligodendrocytes, oligodendrocyte precursor cells (OPCs), vascular leptomeningeal cells (VLMCs) and pericytes. A separate identity was created for fibroblasts as cells which expressed *Col1a2* and *Pdgfrb*, and OPCs as being *Pdgfra* and *Sox6* positive. The FindAllMarkers function with default Wilcoxon rank sum test was used to identify distinguishing markers for each cluster. The DoHeatmap function with downsampling to 1000 was used to generate a heatmap with top 5 genes for each cluster. Data from macrophages, fibroblasts and OPCs from LPC sections were subset from the main dataset and used with the package CellChat v2 to assess ligand-receptor interactions[61]. To assess significant ligand-receptor interactions the computeCommunProb command was used with the following parameters (type="truncatedMean", distance.use=TRUE, contact.dependent=TRUE, contact.range=50).

Analysis of mouse single nuclei dataset from LPC lesions

LPC-lesioned tissue dataset from Melchor et al. (accession number GSE278643) was used to validate fibroblast population increases in LPC. Briefly, processed data were directly downloaded, and all quality control, dimensionality reduction, and clustering were performed using Seurat (v5.1.0) in R (v4.4.1) as per original publication. All samples (naïve spinal cord tissue (n=2), LPC and sham 5dpl (n=3, n=1), 10dpl (n=2, n=1), and 20dpl (n=3, n=1) were utilized. To cluster the data, we used the SCTransform v2 function[62,63]. The count matrix was log normalized using the NormalizeData function to identify cluster gene markers. All cell populations were annotated based off of well-known and calculated marker genes through the

FindAllMarkers function. Vascular and mesenchymal cells (*Pdgfrb*, *Cfap43*, *Pecam1*, *Cspg4*, *Col1a2*) were subset based off marker genes. The subset vascular/mesenchymal dataset was reclustered (65 PCs and resolution = 2.2) and filtered following the original publication, count matrices were renormalized using the NormalizeData function, and clusters were manually annotated based on the expression of cell type-specific genes.

Analysis of publicly available human single nuclei dataset from MS patients

Fastq files from the human MS single nuclei transcriptomic study by Absinta et al. (accession number GSE180759) were downloaded and demultiplexed using 10x Genomics Cellranger version 5.0 pipeline. The final expression matrix with gene counts from n=3 controls and n=5 patients was then analysed using the bioinformatics package Seurat v5[59]. Metadata defining tissue area was included in the object. Before running QC metrics the expression matrix comprised 34,131 features and 134,932 cells. Data was filtered for parameters: gene present in > 3 cells and cells with < 150,000 nCount_RNA and percent of mitochondrial genes < 10%. Post filtering, the expression matrix contained 33,454 features and 128,343 cells. Data was normalized and scaled using the SCTransform v2 function with percent.mt being regressed out. A PCA-reduction was performed and 30 significant dimensions were considered to generate a UMAP with all cells in the dataset. Clusters were determined using the FindClusters function which implements the Louvain algorithm for modularity optimization and with resolution of 0.3. Cluster annotation was done manually based on the expression of lineage specific hallmark genes. Differentially expressed genes for one cluster (versus all cells in other clusters) was determined by the default Wilcoxon rank sum test. PDGFRB+ cells from the initial fibroblast cluster were then subset and re-clustered. Data from microglia/macrophages, OPCs and PDGFRB+ fibroblasts were subset from the main data and used with the package CellChat2 v2 to assess ligand-receptor interactions[61]. To assess significant ligand-receptor interactions the

computeCommunProb command was used with the following parameters (type="truncatedMean", trim = 0.05, population.size=TRUE).

Statistical analysis

Data was collated using Microsoft Excel. Graphs were generated using GraphPad Prism 8. Data shown are the individual data points, whereby each point on a bar graph represents a biological (for in vivo experiments) or technical replicate (for in vitro experiments), and the mean. No statistical methods were used to predetermine sample sizes, but sample sizes were similar to those previously reported[28,55,64]. Experimental groups were randomly assigned. Data collection and analysis were not performed blind to the conditions of the experiment (unless otherwise stated), as all image and data analyses were completed with the same acquisition conditions and analysis thresholds. Statistical tests are listed in figure legends.

Legend to Figures

Fig 1. Fibroblasts localize in LPC demyelinated SCWM. a-d. Immunofluorescence images of day 7 LPC lesions labeled with: **(a)** DAPI, MBP, NFH and GFAP in wildtype mice; **(b)** DAPI, Iba1 and TdTomato (TdTom) in PDGFRβ-TdTom mice; **(c)** DAPI, TdTom and PDGFRβ in PDGFRβ-TdTom mice; **(d)** DAPI, PDGFRβ, COL1A1 and SMA in wildtype mice. Scale bar = 100 μm, inset = 25 μm. **e-j.** Graphs comparing day 7 and day 21 **(e, h)** lesion volume, **(f, i)** TdTom positive volume, **(g, j)** proportion of LPC lesion that is TdTom positive. **k.** Representative images of day 7 and 21 LPC lesions labeling for PDGFRβ-TdTom and **(left)** periostin (POSTN), **(middle)** fibronectin (FN1), and **(right)** SMA. Scale bar = 100 μm. **l-n.** Graphs comparing the proportion of day 7 and 21 lesions positive for **(l)** POSTN, **(m)** FN1, **(n)** SMA. Data was acquired from two experiments; n=8 per experimental group. Significance is indicated as *P<0.05, **P<0.01, ***P<0.001, ****P<0.0001; unpaired *t*-test, comparing day 7 and day 21 LPC lesions. Data presented as the mean.

Fig 2. Single-nucleus RNA sequencing confirms the prominence of fibroblasts in LPC lesions. a. Dotplot of broadly annotated vascular and mesenchymal cell populations highlighting marker genes used for annotation. **B.** UMAP plot of broadly annotated vascular and mesenchymal cell populations (*left*), and at the different timepoints investigated post-demyelination (**c**). **d.** Bar plot showing the relative frequencies of broadly annotated vascular/mesenchymal subpopulations in each experimental timepoint, highlighting the prominence of fibroblasts in lesioned samples.

Fig 3. Spatial transcriptomics of fibroblasts in demyelinated lesions. **a, b.** Representative images of annotated cells in **(a)** sham and **(b)** LPC demyelinated spinal cords at 14 dpi. Lesion edge indicated by white dashed line. **c, d.** UMAP visualization of 2954 cells from LPC and sham colored by **(c)** experimental group and **(d)** mapped cell clusters (20 principal components, resolution=0.7). **e.** Heatmap of top 5 differentially expressed genes across annotated cell

groups as determined using FindAllMarkers (default Wilcoxon Rank Sum test, min. logfc threshold = 0.25). **f, g.** Bar graph showing **(f)** the total number of cells, and **(g)** the fold change in cell groups between LPC and sham groups. Abbreviations: M/M – microglia/macrophages; OL – oligodendrocytes; OPCs – oligodendrocyte precursor cells; EC – endothelial cells; VLMC – vascular leptomeningeal cells.

Fig 4. Inferred Incoming and outgoing signaling patterns between fibroblasts, OPCs and macrophages in day 14 LPC lesions. Heatmap of **(a)** inferred outgoing and **(b)** incoming signaling pathways as assessed for the 3 cell groups. Color bar in the heatmap represents the relative signaling strength of a pathway across all cell groups (values are row-scaled). Top colored bar plot shows the total signaling strength of a cell group by summarizing all pathways displayed in the heatmap. The right grey bar plot shows the total signaling strength of a pathway by summarizing all cell groups displayed in the heatmap. Heatmap of **(c)** outgoing and **(e)** incoming signaling pathways that contribute to each communication pattern. River plots showing the cell source for **(d)** outgoing and **(f)** incoming communication patterns and the pathways associated with them. The thickness of the flow indicates contribution of cell group or signaling pathway to each pattern.

Fig 5. Post inflammation fibroblast response stimulated by microglia/macrophages. **a, b.** Representative image of **(a)** day 3 and **(b)** day 7 LPC lesion labelling for DAPI, PDGFRβ, and Iba1. Scale bar = 100 μm. **b.** Representative images of LPC lesioned SCWM day 3, 7, 14, and 21 day post injury labelling for DAPI, PDGFRβ, and Iba1. Scale bar = 100 μm (insert = 25 μm). **c, d.** Graphs indicating day 3, 7, 14, and 21 day **(c)** Iba1 positive % area of lesion and **(d)** PDGFRβ positive % area of lesion. **e.** Schematic of experimental design. Meningeal fibroblasts were added to upper compartment and BMDMs or medium alone added to the lower compartment. **f.** Representative images of hematoxylin stained transwell inserts from BMDM and medium control groups. **g.** Graph comparing the amount of hematoxylin stained meningeal

fibroblasts migrated across the transwell membrane in BMDM and medium alone control. **(c, d)** n=5 (D3), 10 (D7), 7 (D14), 5 (D21); **(g)** n = 4 for each experimental group; Significance indicated as *P<0.05, **P<0.01, one-way ANOVA comparing time points (D3, 7, 14, or 21) **(c, d)**; or two-tailed unpaired *t*-test **(g).** All data presented as the mean.

Fig 6. Fibroblasts spatially exclude OPCs in LPC lesions and in vitro. **a.** Representative images of day 14 LPC lesion stained for PDGFRβ, Olig2, and PDGFRα. **b.** Representative images of day 14 LPC lesion in NG2CreER:MAPTmGFP mice labelling for DAPI, PDGFRβ, NG2-GFP. **c.** Graph comparing GFP positive area in day 14 LPC lesions. PDGFRβ positive area of LPC lesion (red) and PDGFRβ negative area of LPC lesion (white). n = 9 , Significance indicated ***P<0.001, two-tailed unpaired *t*-test. Data presented as mean. **d.** Representative image of OPC alone (left) and OPC-fibroblast co-cultures (right) labelled for nuclei (blue), O4 (green), MBP (red), and PDGFRβ (white). **e-g.** Graphs indicating fold change in **(e)** O4 positive OPCs, **(f)** O4 positive MBP positive mature oligodendrocytes, and **(g)** mean processes per cell comparing co-cultures with OPC alone controls. n = 2 independent experiments with 4 replicates for e-g. Significance indicated as *P<0.05, **P<0.01, two-tailed, unpaired *t*-test, Data presented as mean.

Fig 7. Age exacerbates fibroblast response to demyelination. **a.** Representative immunofluorescence images of day 7 LPC lesions in young and middle-aged mice labeled with DAPI and MBP (red) or PDGFRβ (white). Lesion is indicated with white dashed line. **b-f.** Graphs comparing spinal cord spread of **(b, d)** total lesion volume, **(c, e)** PDGFRβ positive immunofluorescence, and **(f)** proportion of lesion volume that is PDGFRβ positive at days 7, 14, and 21 after LPC injury. For young group, n = 4 (D7), 4 (D14), 5 (D21; for middle-aged group n = 5 for each time point. Significance is indicated as *P<0.05, **P<0.01; unpaired, *t*-test, comparing young and middle-aged groups. Data is presented as the mean.

Fig 8. Age enhances fibroblast properties in demyelinated lesions. **a.** Representative immunofluorescence images of day 7 LPC lesions in young and middle-aged mice labeled for DAPI, PDGFRβ and SMA; and quantification of the proportion of PDGFRβ overlapping with SMA at 7 and 21 dpi in young and middle-aged mice. **b.** Representative immunofluorescence images of day 7 LPC lesion of young mice labeled for DAPI, PDGFRβ, and Col1a1; and quantification of Col1a1 positive area at 7 and 21 dpi in young and middle-aged mice. **c.** Representative immunofluorescence images of day 7 LPC lesion in young mice labeled for DAPI and LAMA (laminin); and quantification of LAMA positive area at 7 and 21 dpi in young and middle-aged mice. **d.** Representative immunofluorescence images of day 7 LPC lesion in young mice labeled for DAPI, Olig2, and PDGFRβ; graphs comparing the number of Olig2 positive cells within PDGFRβ positive regions of the LPC lesion at 7 and 21 days post LPC injury. In the graphs, each dot is an individual mouse. Significance is indicated as *P<0.05, **P<0.01, ***P<0.001; unpaired, *t*-test, comparing young and middle-aged groups. Data presented as mean.

Fig 9. Fibroblasts in MS lesions. **a.** Representative immunofluorescence images of MS lesions labeled for DAPI, CD45, and PDGFRβ. This is observed in 5 different MS cases (not shown). **b.** UMAP visualization of 66,432 cells from MS lesions and their cell annotation[39]. **c.** Dot plot indicating markers used to identify fibroblast population. Size of the dot indicates the percentage of cells while the color encodes the average expression levels across all cells. **d.** Violin plots depicting log normalized gene expression of fibroblast markers comparing PDGFRβ positive fibroblast population to other cell groups. **e, f.** UMAP visualization of **(e)** subclusters of PDGFRβ positive fibroblast population with top 10 DEGs, and **(f)** distribution of PDGFRβ positive fibroblast subclusters across MS lesion types and frontal white matter from neurologically normal controls.

Fig 10. Fibroblast interactions in MS lesions. **a, b.** Heatmap and river plots indicating cell and signaling pathways associated with outgoing and incoming communication patterns in MS lesions. The thickness of the flow indicates contribution of cell group or signaling pathway to each pattern. **c, d.** Venn diagrams of (l) outgoing and (m) incoming signaling pathways comparing MS and LPC lesions.

Legend to Supplementary figures

Supp Fig 1. Ligand – receptor (L-R) interactions between fibroblasts, OPCs, and microglia/macrophages in day 14 LPC lesions (related to main Figure 4). a, c. Number of significant ligand-receptor between any pair of two cell populations shown as **(a)** circle plot and **(c)** heatmap. **b, d.** Interaction strength between ligand-receptor of any pair of two cell populations shown as **(b)** circle plot and **(d)** heatmap. In the circle plots, the circle sizes are proportional to the number of cells in each group; edge weights are proportional to the interaction strength. **e. Scatter plot** of incoming and outgoing interaction strength showing fibroblasts as major outgoing signaling source. Dot size is proportional to the number of inferred links (outgoing and incoming) associated with each cell group. **f, g**. Chord plot showing L-R interactions with fibroblasts as **(f)** source of signal.

Supp Fig 2. Incoming and outgoing fibroblast L-R interactions in day 14 LPC lesions (related to main Figure 4). a, b. Bubble plot delineating L-R interactions from one cell group (i.e. sender) to another (i.e. target) as indicated in the plot.

Supp Fig 3. Cell contributions to communication networks (related to main Figure 4). a, b. Dot plots indicating cell type contribution to **(a)** outgoing and **(b)** incoming communication patterns.

Supp Fig 4. Axon densities are unchanged in fibroblast occupied regions. a. Representative image of a day 21 LPC lesion stained for DAPI, NFH, and PDGFRβ. **b.** Quantification comparing NFH positive axon density in fibroblast occupied areas with the rest of the LPC lesion. Sample sizes n = 7 across two experiments. Two-tailed, unpaired *t*-test comparing groups. Data are the mean ± s.d.

Supp Fig 5. Fibroblast density is associated with reduced OPC maturation (related to main Figure 5). a. Quantification of total DAPI+ cells with 10, 100, 1k, 10k, 100k fibroblasts added. **b.** Mean outgrowth per cell with 10, 100, 1k, 10k, 100k fibroblasts added. **c.** Graphs comparing OPCs cultured alone, with fibroblast conditioned medium (CM), or with fibroblasts showing mean outgrowth per cell. **d.** Graphs comparing OPCs cultured alone, added before fibroblasts, and added after fibroblasts showing mean outgrowth per cell. Significance is indicated as *P < 0.05, **P < 0.01, ***P < 0.001, ****P < 0.0001. Sample sizes n = as shown number of technical replicates. Kruskal-Wallis followed by a Dunn's multiple comparisons. Mean shown as horizontal line.

Supp Fig 6. Main cell types as assessed in MS lesions (related to main Figure 9). a. Heatmap of top 5 differentially expressed genes across annotated cell groups.

Supp Fig 7. Non-fibroblast related marker expression across cell clusters assessed in MS lesions (related to main Figure 9). a. Violin plots of *TAGLN* and *RGS5* normalised gene expression in snRNAseq dataset. **b, c.** String-db plot of DEG between fibroblast **(b)** subcluster 0, and **(c)** subclusters 1.

Supp Fig 8. L-R interactions between fibroblasts, M/M and OPcs in MS lesions (related to main Figure 10). a, c. Number of significant ligand-receptor between any pair of two cell populations shown as **(a)** circle plot and **(c)** heatmap. **b, d.** Interaction strength between ligand-receptor any pair of two cell populations shown as **(b)** circle plot and **(d)** heatmap. In the circle

plots, the circle sizes are proportional to the number of cells in each group; edge weights are proportional to the interaction strength. **e.** Schematic indicating inferred outgoing and incoming fibroblast signals and their distribution across signaling databases. **f, g.** Chord plot showing L-R interactions with fibroblasts as **(f)** source of signals, and **(g)** receiver of signals.

Supp Fig 9. Inferred Fibroblast communication patterns in MS (related to main Figure 10). a, b. Bubble plots delineating L-R interactions from one cell group (i.e. sender) to another (i.e. target) as assessed with different signaling databases indicated in the plot **(a)** ECM-receptor and **(b)** secreted signaling databases. **c, d.** Dot plots of **(c)** outgoing and **(d)** incoming communication patterns.

Supp Fig 10. Inferred Communication pattern contributions in MS lesions (related to main Figure 10) a, b. Heatmap of **(a)** inferred outgoing and **(b)** incoming signaling pathways as assessed for the 3 cell groups. Colour bar in the heatmap represents the relative signaling strength of a pathway across all cell groups (values are row-scaled). Top colored bar plot shows the total signaling strength of a cell group by summarizing all pathways displayed in the heatmap. The right grey bar plot shows the total signaling strength of a pathway by summarizing all cell groups displayed in the heatmap. **c, d.** Venn-diagrams comparing LPC (CosMx) and MS (snRNAseq) **(c)** outgoing and **(d)** incoming fibroblast L-R interactions.

References

1. Plikus, M. V. *et al.* Fibroblasts: Origins, definitions, and functions in health and disease. *Cell* **184**, 3852–3872 (2021).
2. Zhou, X. *et al.* Microenvironmental sensing by fibroblasts controls macrophage population size. *Proc Natl Acad Sci U S A* **119**, e2205360119 (2022).
3. Plikus, M. V. *et al.* Regeneration of fat cells from myofibroblasts during wound healing. *Science* **355**, 748–752 (2017).
4. Dorrier, C. E., Jones, H. E., Pintarić, L., Siegenthaler, J. A. & Daneman, R. Emerging roles for CNS fibroblasts in health, injury and disease. *Nature Reviews Neuroscience* **23**, 23–34 (2022).
5. Dorrier, C. E. *et al.* CNS fibroblasts form a fibrotic scar in response to immune cell infiltration. *Nature Neuroscience* **24**, 234–244 (2021).
6. Bolte, A. C. *et al.* The meningeal transcriptional response to traumatic brain injury and aging. *eLife* **12**, 1–38 (2023).
7. Yahn, S. L. *et al.* Neurobiology of Disease Fibrotic scar after experimental autoimmune encephalomyelitis inhibits oligodendrocyte di ff erentiation. *Neurobiology of Disease* **134**, 104674 (2020).
8. Liu, X. *et al.* Reactive Fibroblasts in Response to Optic Nerve Crush Injury. *Mol Neurobiol* **58**, 1392–1403 (2021).
9. Şekerdağ-Kılıç, E. *et al.* Perivascular PDGFRB+ cells accompany lesion formation and clinical evolution differentially in two different EAE models. *Mult Scler Relat Disord* **69**, 104428 (2023).
10. Goritz, C. *et al.* A Pericyte Origin of Spinal Cord Scar Tissue. *Science* **333**, 238–243 (2011).
11. Dias, D. O. *et al.* Reducing Pericyte-Derived Scarring Promotes Recovery after Spinal Cord Injury. *Cell* **173**, 153–165 (2018).

12. Dias, D. O. *et al.* Pericyte-derived fibrotic scarring is conserved across diverse central nervous system lesions. *Nat Commun* **12**, 5501 (2021).
13. Franklin, R. J. M. & Simons, M. CNS remyelination and inflammation: From basic mechanisms to therapeutic opportunities. *Neuron* **110**, 3549–3565 (2022).
14. Lubetzki, C., Zalc, B., Williams, A., Stadelmann, C. & Stankoff, B. Remyelination in multiple sclerosis : from basic science to clinical translation. *The Lancet Neurology* **19**, 678–688 (2020).
15. Mei, F. *et al.* Accelerated remyelination during inflammatory demyelination prevents axonal loss and improves functional recovery. *eLife* **5**, 1–21 (2016).
16. Ghorbani, S. *et al.* Versican promotes T helper 17 cytotoxic inflammation and impedes oligodendrocyte precursor cell remyelination. *Nature Communications* **13**, 1–18 (2022).
17. Rawji, K. S. *et al.* Niacin-mediated rejuvenation of macrophage/microglia enhances remyelination of the aging central nervous system. *Acta Neuropathologica* **139**, 893–909 (2020).
18. Dong, Y. *et al.* Single-cell and spatial RNA sequencing identify perturbators of microglial functions with aging. *Nature Aging* (2022) doi:10.1038/s43587-022-00205-z.
19. Koch, M., Mostert, J., Heersema, D. & De Keyser, J. Progression in multiple sclerosis: Further evidence of an age dependent process. *Journal of the Neurological Sciences* **255**, 35–41 (2007).
20. Brack, A. S. *et al.* Increased Wnt signaling during aging alters muscle stem cell fate and increases fibrosis. *Science* **317**, 807–810 (2007).
21. Chambers, E. S. *et al.* Recruitment of inflammatory monocytes by senescent fibroblasts inhibits antigen-specific tissue immunity during human aging. *Nature Aging* **1**, (2021).
22. Salzer, M. C. *et al.* Identity Noise and Adipogenic Traits Characterize Dermal Fibroblast Aging. *Cell* **175**, 1575-1590.e22 (2018).

23. Mahmoudi, S. *et al. Heterogeneity in Old Fibroblasts Is Linked to Variability in Reprogramming and Wound Healing*. *Nature* vol. 574 (Springer US, 2019).
24. Shen, S. *et al.* Age-dependent epigenetic control of differentiation inhibitors is critical for remyelination efficiency. *Nature Neuroscience* **11**, 1024–1034 (2008).
25. Nicaise, A. M. *et al.* Cellular senescence in progenitor cells contributes to diminished remyelination potential in progressive multiple sclerosis. *Proceedings of the National Academy of Sciences of the United States of America* **116**, 9030–9039 (2019).
26. Neumann, B. *et al.* Metformin Restores CNS Remyelination Capacity by Rejuvenating Aged Stem Cells. *Cell Stem Cell* **25**, 473-485.e8 (2019).
27. Anderson, M. A. *et al.* Astrocyte scar formation aids central nervous system axon regeneration. *Nature* **532**, 195–200 (2016).
28. Plemel, J. R. *et al.* Microglia response following acute demyelination is heterogeneous and limits infiltrating macrophage dispersion. *Science Advances* **6**, eaay6324 (2020).
29. Lozinski, B. M. *et al.* Exercise rapidly alters proteomes in mice following spinal cord demyelination. *Scientific Reports* **11**, (2021).
30. Henderson, N. C. *et al.* Targeting of αv integrin identifies a core molecular pathway that regulates fibrosis in several organs. *Nature Medicine* **19**, 1617–1624 (2013).
31. Buhl, E. M. *et al.* Dysregulated mesenchymal PDGFR-β drives kidney fibrosis. *EMBO Molecular Medicine* **12**, (2020).
32. Holl, D. *et al.* Distinct origin and region-dependent contribution of stromal fibroblasts to fibrosis following traumatic injury in mice. *Nat Neurosci* (2024) doi:10.1038/s41593-024-01678-4.
33. Melchor, G. S., Baydyuk, M., Manavi, Z., Hu, J. & Huang, J. K. Dissecting the evolving cellular landscape of a remyelinating microenvironment. 2024.12.25.630253 Preprint at https://doi.org/10.1101/2024.12.25.630253 (2024).

34. Jensen, S. K. *et al.* Multimodal Enhancement of Remyelination by Exercise with a Pivotal Role for Oligodendroglial PGC1α. *Cell Reports* **24**, 3167–3179 (2018).
35. Jin, S. *et al.* Inference and analysis of cell-cell communication using CellChat. *Nat Commun* **12**, 1088 (2021).
36. López-Otín, C., Blasco, M. A., Partridge, L., Serrano, M. & Kroemer, G. Hallmarks of aging: An expanding universe. *Cell* **186**, 243–278 (2023).
37. Segel, M. *et al.* Niche stiffness underlies the ageing of central nervous system progenitor cells. *Nature* **573**, 130–134 (2019).
38. Goldschmidt, T., Antel, J., Konig, F. B., Bruck, W. & Kuhlmann, T. Remyelination capacity of the MS brain decreases with disease chronicity. *Neurology* **72**, 1914–1921 (2009).
39. Absinta, M. *et al.* A lymphocyte – microglia – astrocyte axis in chronic active multiple sclerosis. *Nature* (2021) doi:10.1038/s41586-021-03892-7.
40. Yang, A. C. *et al.* A human brain vascular atlas reveals diverse mediators of Alzheimer's risk. *Nature* **603**, 885–892 (2022).
41. Vanlandewijck, M. *et al.* A molecular atlas of cell types and zonation in the brain vasculature. *Nature* **554**, 475–480 (2018).
42. Cregg, J. M. *et al.* Functional Regeneration Beyond the Glial Scar. *Exp Neurol* **0**, 197–207 (2014).
43. Bernier, L.-P. *et al.* Brain pericytes and perivascular fibroblasts are stromal progenitors with dual functions in cerebrovascular regeneration after stroke. *Nat Neurosci* **28**, 517–535 (2025).
44. Rustenhoven, J. *et al.* Functional characterization of the dural sinuses as a neuroimmune interface. *Cell* **184**, 1000-1016.e27 (2021).
45. Donovan, J., Shiwen, X., Norman, J. & Abraham, D. Platelet-derived growth factor alpha and beta receptors have overlapping functional activities towards fibroblasts. *Fibrogenesis Tissue Repair* **6**, 10 (2013).

46. Zhou, X. *et al.* Circuit Design Features of a Stable Two-Cell System. *Cell* **172**, 744-757.e17 (2018).

47. Adler, M. *et al.* Principles of Cell Circuits for Tissue Repair and Fibrosis. *iScience* **23**, 100841 (2020).

48. Stephenson, E. L. *et al.* Chondroitin sulfate proteoglycans as novel drivers of leucocyte infiltration in multiple sclerosis. *Brain* 1094–1110 (2018) doi:10.1093/brain/awy033.

49. Ghorbani, S. & Yong, V. W. The extracellular matrix as modifier of neuroinflammation and remyelination in multiple sclerosis. *Brain* **144**, 1958–1973 (2021).

50. Wang, F. *et al.* Myelin degeneration and diminished myelin renewal contribute to age-related deficits in memory. *Nature Neuroscience* **23**, 481–486 (2020).

51. Shields, S. A., Gilson, J. M., Blakemore, W. F. & Franklin, R. J. M. Remyelination occurs as extensively but more slowly in old rats compared to young rats following gliotoxin-induced CNS demyelination. *Glia* **28**, 77–83 (1999).

52. Rawji, K. S. *et al.* Immunosenescence of microglia and macrophages: Impact on the ageing central nervous system. *Brain* **139**, 653–661 (2016).

53. Müller, L. & Di Benedetto, S. Aging brain: exploring the interplay between bone marrow aging, immunosenescence, and neuroinflammation. *Front Immunol* **15**, 1393324 (2024).

54. Hoeft, K. *et al.* Platelet-instructed SPP1+ macrophages drive myofibroblast activation in fibrosis in a CXCL4-dependent manner. *Cell Reports* **42**, 112131 (2023).

55. Dong, Y. *et al.* Oxidized phosphatidylcholines found in multiple sclerosis lesions mediate neurodegeneration and are neutralized by microglia. *Nature Neuroscience* **24**, 489–503 (2021).

56. Keough, M. B., Jensen, S. K. & Wee Yong, V. Experimental demyelination and remyelination of murine spinal cord by focal injection of lysolecithin. *Journal of Visualized Experiments* **2015**, 1–8 (2015).

57. He, S. *et al.* High-plex imaging of RNA and proteins at subcellular resolution in fixed tissue by spatial molecular imaging. *Nat Biotechnol* **40**, 1794–1806 (2022).
58. Stringer, C., Wang, T., Michaelos, M. & Pachitariu, M. Cellpose: a generalist algorithm for cellular segmentation. *Nat Methods* **18**, 100–106 (2021).
59. Hao, Y. *et al.* Dictionary learning for integrative, multimodal and scalable single-cell analysis. *Nat Biotechnol* **42**, 293–304 (2024).
60. Korsunsky, I. *et al.* Fast, sensitive and accurate integration of single-cell data with Harmony. *Nat Methods* **16**, 1289–1296 (2019).
61. Jin, S., Plikus, M. V. & Nie, Q. CellChat for systematic analysis of cell–cell communication from single-cell transcriptomics. *Nat Protoc* **20**, 180–219 (2025).
62. Hafemeister, C. & Satija, R. Normalization and variance stabilization of single-cell RNA-seq data using regularized negative binomial regression. *Genome Biol* **20**, 296 (2019).
63. Choudhary, S. & Satija, R. Comparison and evaluation of statistical error models for scRNA-seq. *Genome Biol* **23**, 27 (2022).
64. Jain, R. W., Elliott, D. A. & Yong, V. W. Single Cell Analysis of High-Parameter Histology Images Using Histoflow Cytometry. *The Journal of Immunology* **210**, 2038–2049 (2023).

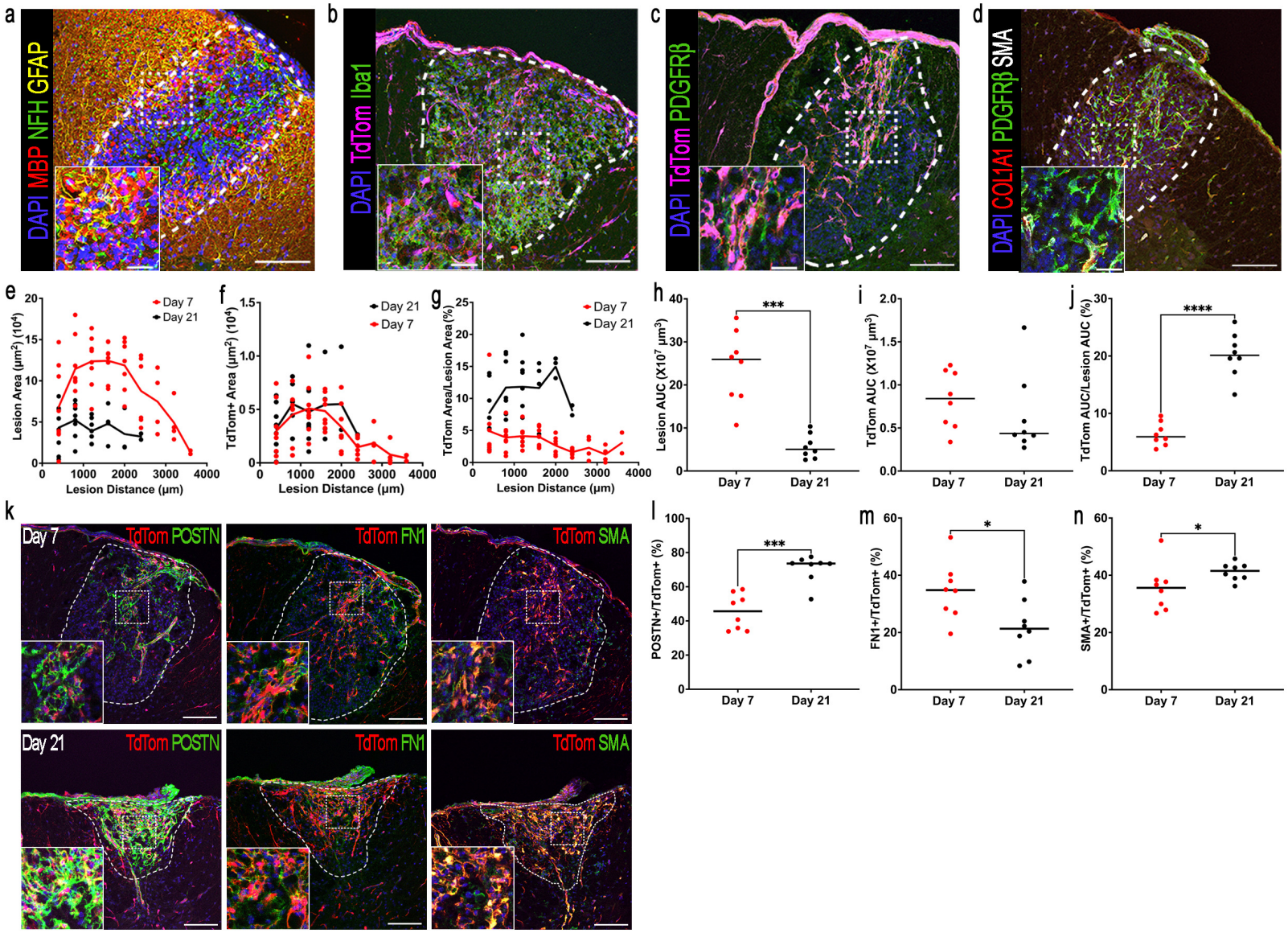
a
DAPI MBP NFH GFAP
b
DAPI TdTom Iba1
c
DAPI TdTom PDGFRβ
d
DAPI COL1A1 PDGFRβ SMA
e
Day 7
Day 21
Lesion Area (μm²) (10⁴)
Lesion Distance (μm)
f
Day 21
Day 7
TdTom+ Area (μm²) (10⁴)
Lesion Distance (μm)
g
Day 7
Day 21
TdTom Area/Lesion Area (%)
Lesion Distance (μm)
h
***
Lesion AUC (X10⁷ μm³)
Day 7
Day 21
i
TdTom AUC (X10⁷ μm³)
Day 7
Day 21
j
****
TdTom AUC/Lesion AUC (%)
Day 7
Day 21
k
Day 7
TdTom POSTN
TdTom FN1
TdTom SMA
Day 21
TdTom POSTN
TdTom FN1
TdTom SMA
l
***
POSTN+/TdTom+ (%)
Day 7
Day 21
m
*
FN1+/TdTom+ (%)
Day 7
Day 21
n
*
SMA+/TdTom+ (%)
Day 7
Day 21

Fig 1

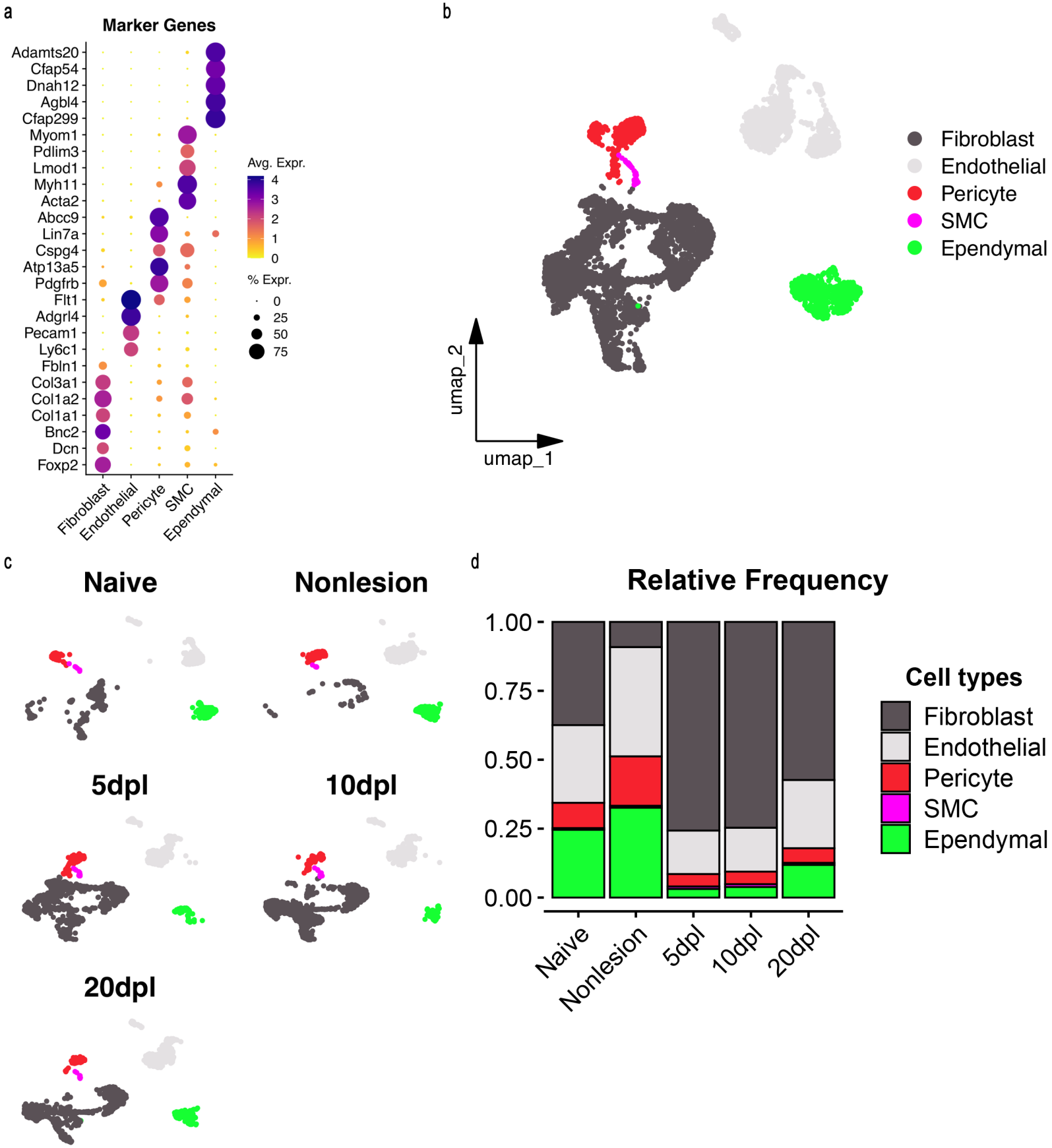
a
Marker Genes
Adamts20
Cfap54
Dnah12
Agbl4
Cfap299
Myom1
Pdlim3
Lmod1
Myh11
Acta2
Abcc9
Lin7a
Cspg4
Atp13a5
Pdgfrb
Flt1
Adgrl4
Pecam1
Ly6c1
Fbln1
Col3a1
Col1a2
Col1a1
Bnc2
Dcn
Foxp2
Fibroblast
Endothelial
Pericyte
SMC
Ependymal
Avg. Expr.
4
3
2
1
0
% Expr.
0
25
50
75
b
umap_2
umap_1
Fibroblast
Endothelial
Pericyte
SMC
Ependymal
c
Naive
Nonlesion
5dpl
10dpl
20dpl
d
Relative Frequency
1.00
0.75
0.50
0.25
0.00
Naive
Nonlesion
5dpl
10dpl
20dpl
Cell types
Fibroblast
Endothelial
Pericyte
SMC
Ependymal

Fig 2

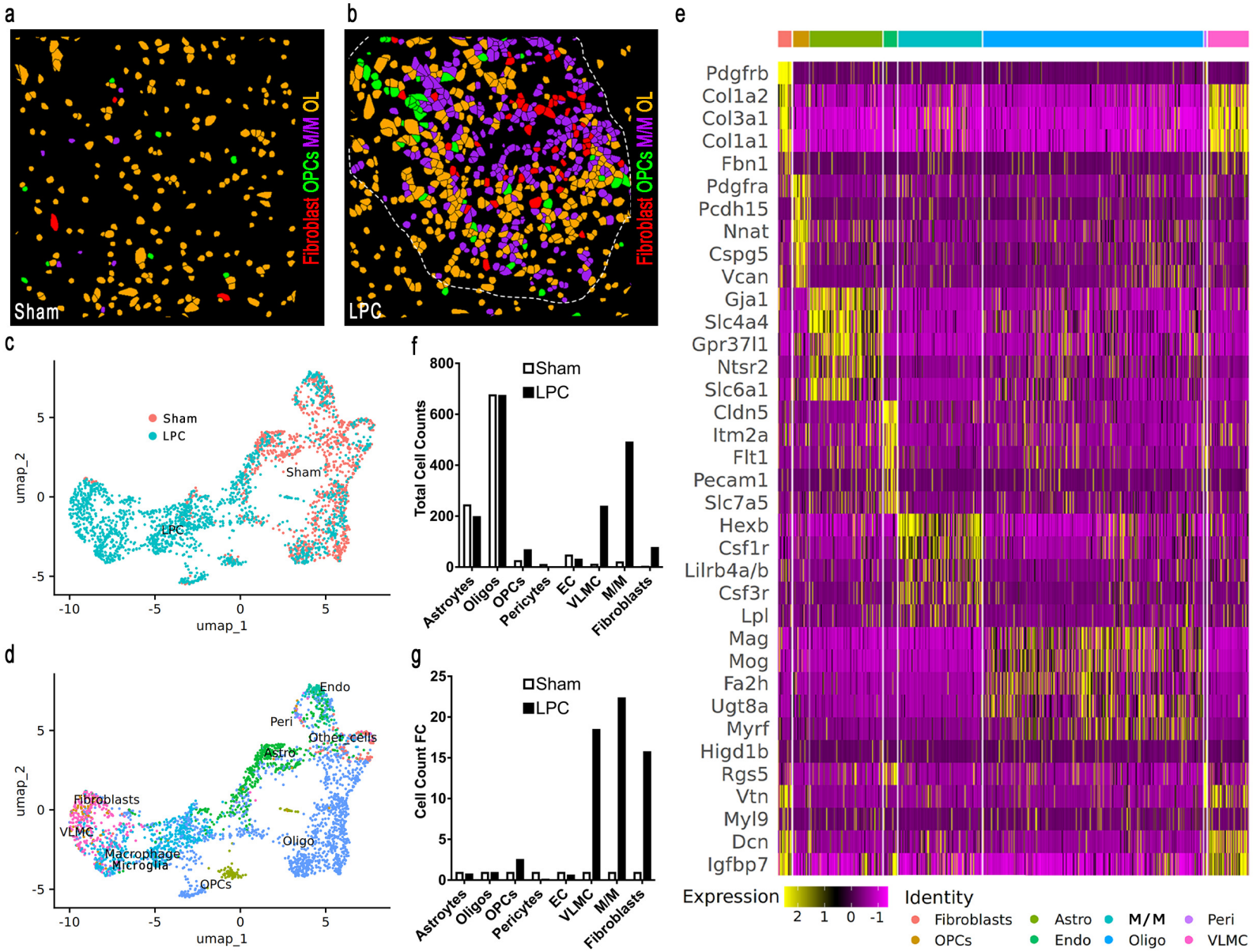
a
Sham
Fibroblast OPCs M/M OL
b
LPC
Fibroblast OPCs M/M OL
c
Sham
LPC
umap_2
umap_1
d
Endo
Peri
Other_cells
Astro
Fibroblasts
VLMC
Macrophage
Microglia
OPCs
Oligo
umap_2
umap_1
f
Sham
LPC
Total Cell Counts
Astroytes
Oligos
OPCs
Pericytes
EC
VLMC
M/M
Fibroblasts
g
Sham
LPC
Cell Count FC
Astroytes
Oligos
OPCs
Pericytes
EC
VLMC
M/M
Fibroblasts
e
Pdgfrb
Col1a2
Col3a1
Col1a1
Fbn1
Pdgfra
Pcdh15
Nnat
Cspg5
Vcan
Gja1
Slc4a4
Gpr37l1
Ntsr2
Slc6a1
Cldn5
Itm2a
Flt1
Pecam1
Slc7a5
Hexb
Csf1r
Lilrb4a/b
Csf3r
Lpl
Mag
Mog
Fa2h
Ugt8a
Myrf
Higd1b
Rgs5
Vtn
Myl9
Dcn
Igfbp7
Expression
Identity
Fibroblasts
Astro
M/M
Peri
OPCs
Endo
Oligo
VLMC

Fig 3

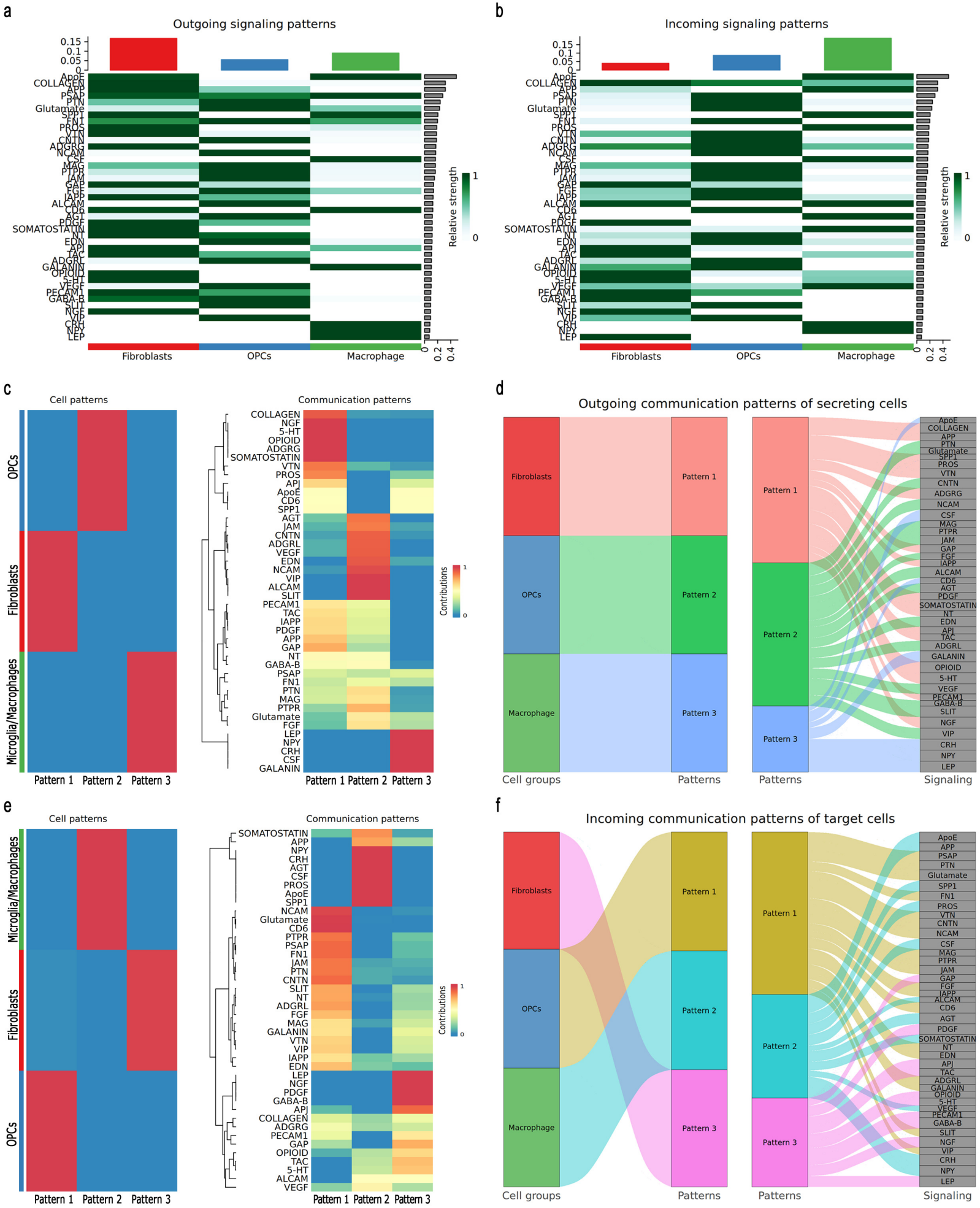
a
Outgoing signaling patterns
Relative strength
Fibroblasts
OPCs
Macrophage
b
Incoming signaling patterns
Relative strength
Fibroblasts
OPCs
Macrophage
c
Cell patterns
Communication patterns
OPCs
Fibroblasts
Microglia/Macrophages
Pattern 1
Pattern 2
Pattern 3
Contributions
d
Outgoing communication patterns of secreting cells
Fibroblasts
OPCs
Macrophage
Pattern 1
Pattern 2
Pattern 3
Cell groups
Patterns
Signaling
e
Cell patterns
Communication patterns
Microglia/Macrophages
Fibroblasts
OPCs
Pattern 1
Pattern 2
Pattern 3
Contributions
f
Incoming communication patterns of target cells
Fibroblasts
OPCs
Macrophage
Pattern 1
Pattern 2
Pattern 3
Cell groups
Patterns
Signaling

Fig 4

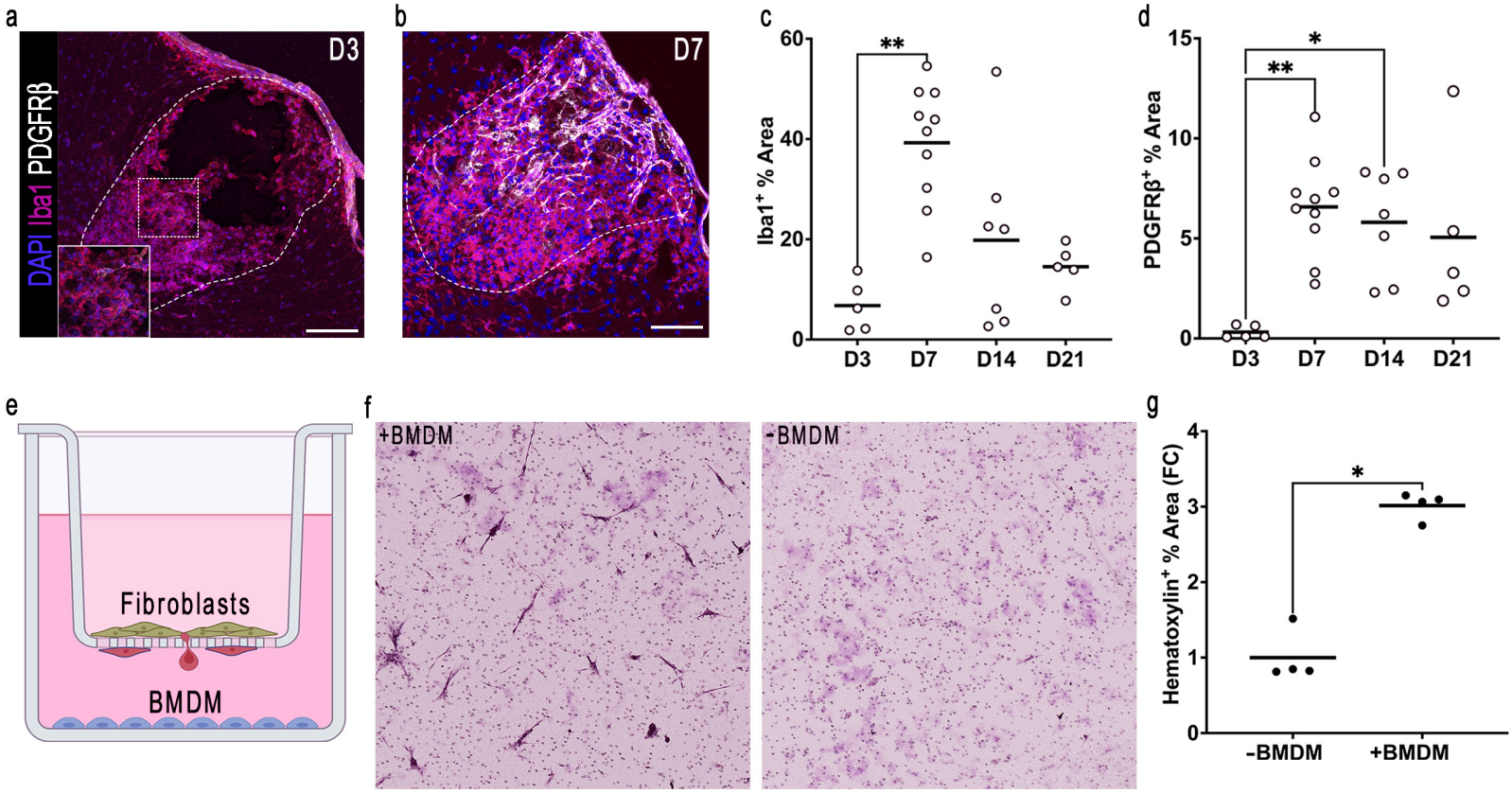
a
DAPI Iba1 PDGFRβ
D3
b
D7
c
Iba1+ % Area
60
40
20
0
**
D3
D7
D14
D21
d
PDGFRβ+ % Area
15
10
5
0
*
**
D3
D7
D14
D21
e
Fibroblasts
BMDM
f
+BMDM
-BMDM
g
Hematoxylin+ % Area (FC)
4
3
2
1
0
*
-BMDM
+BMDM

Fig 5

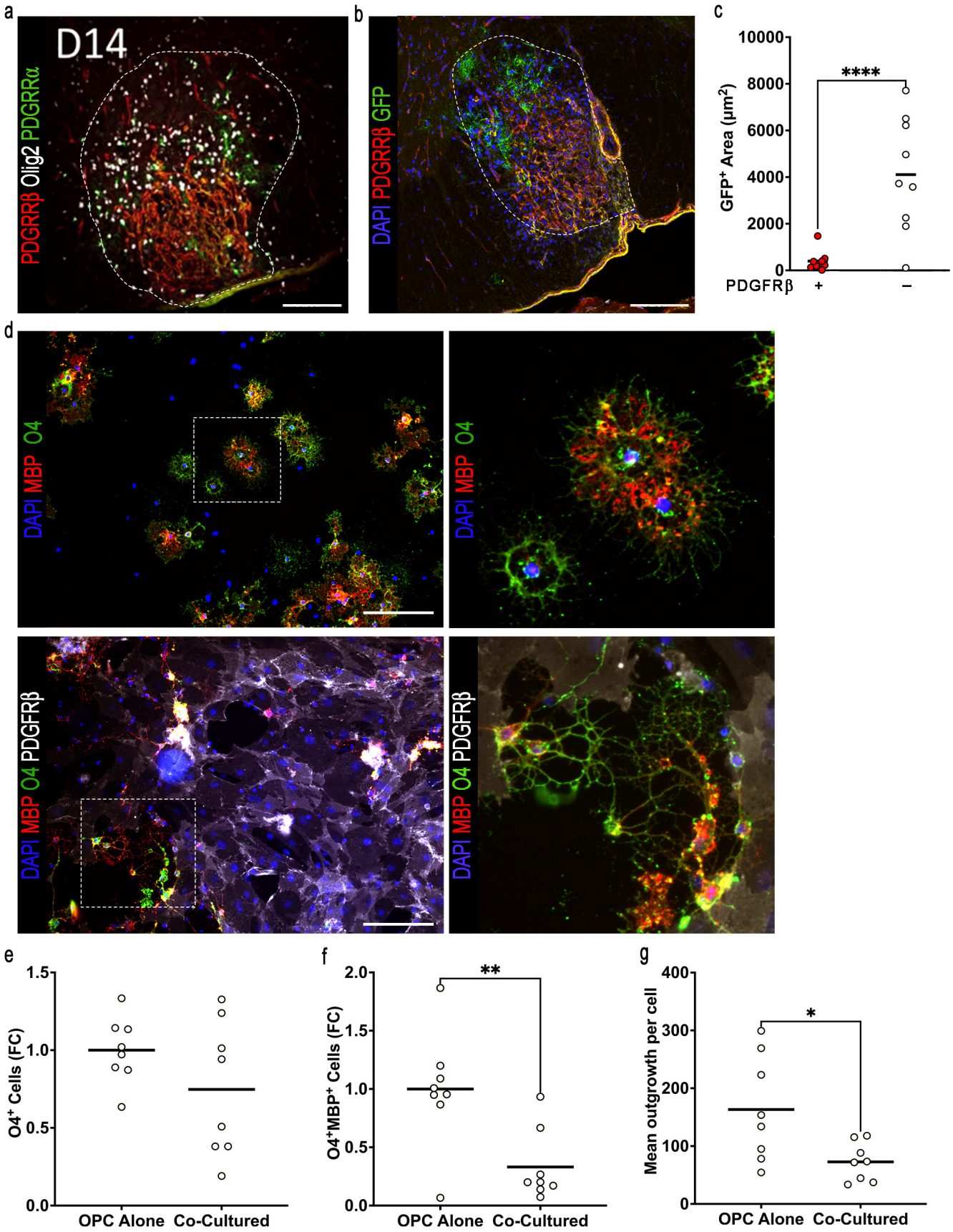
a
D14
PDGRRβ Olig2 PDGRRα
b
DAPI PDGRRβ GFP
c
GFP+ Area (μm2)
10000
8000
6000
4000
2000
0
****
PDGFRβ
+
−
d
DAPI MBP O4
DAPI MBP O4
DAPI MBP O4 PDGFRβ
DAPI MBP O4 PDGFRβ
e
O4+ Cells (FC)
1.5
1.0
0.5
0.0
OPC Alone
Co-Cultured
f
O4+MBP+ Cells (FC)
2.0
1.5
1.0
0.5
0.0
**
OPC Alone
Co-Cultured
g
Mean outgrowth per cell
400
300
200
100
0
*
OPC Alone
Co-Cultured

Fig 6

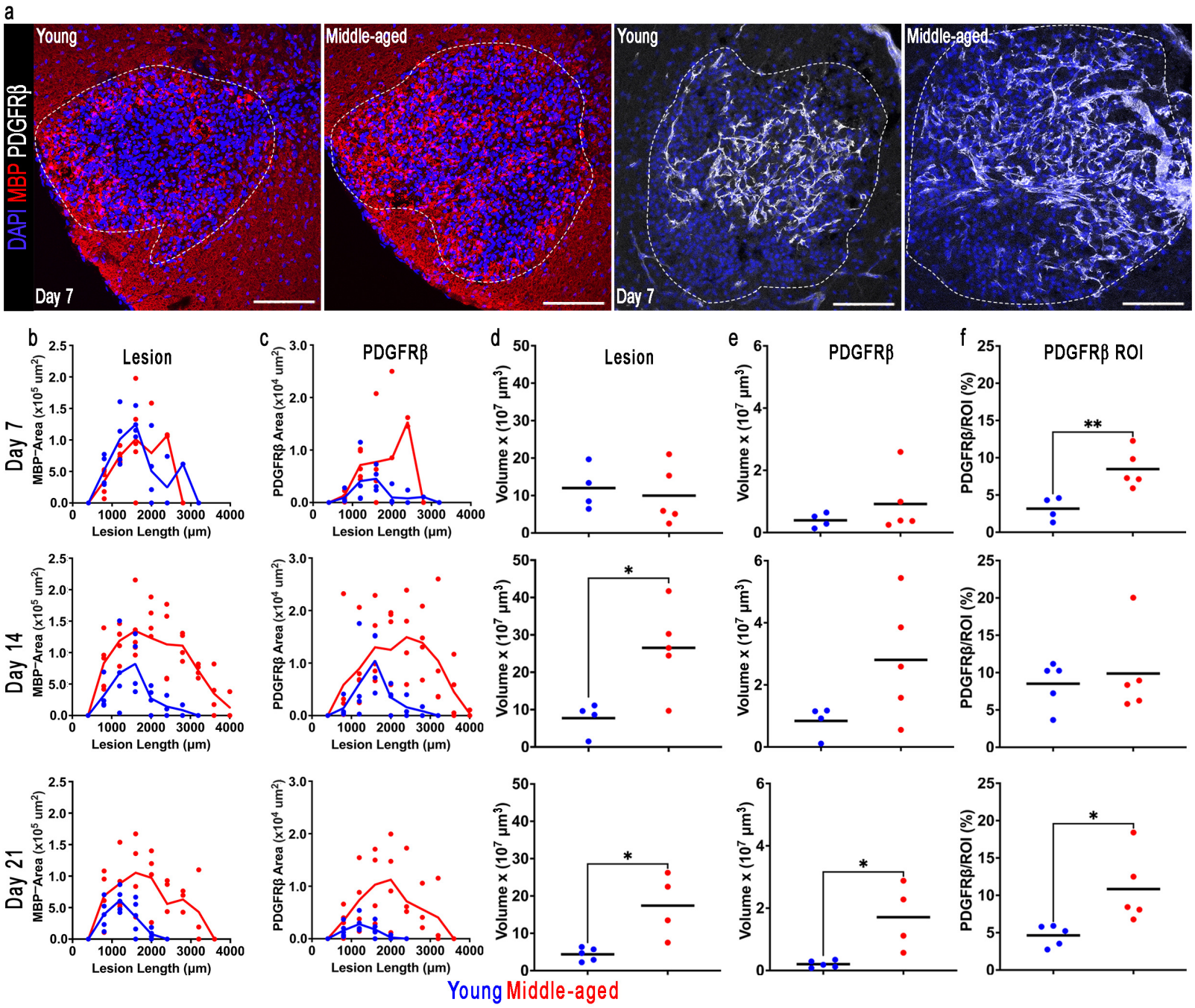
a
Young
Middle-aged
Young
Middle-aged
DAPI MBP PDGFRβ
Day 7
Day 7
b
Lesion
c
PDGFRβ
d
Lesion
e
PDGFRβ
f
PDGFRβ ROI
Day 7
Day 14
Day 21
MBP−Area (x10^5 um^2)
PDGFRβ Area (x10^4 um^2)
Volume x (10^7 μm^3)
PDGFRβ/ROI (%)
Lesion Length (μm)
*
**
Young Middle-aged

Fig 7

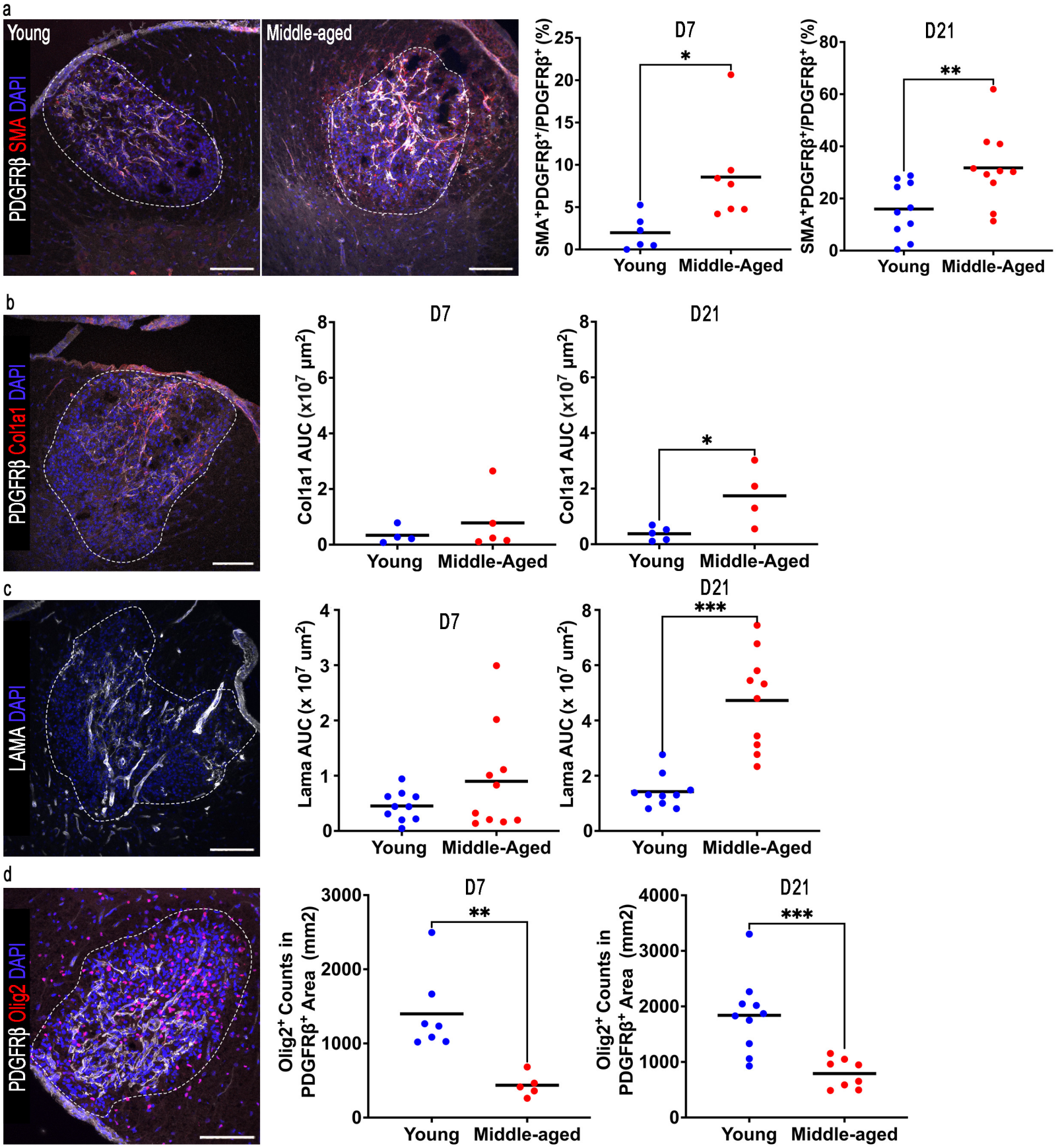
a
Young
Middle-aged
PDGFRβ SMA DAPI
D7
D21
SMA+PDGFRβ+/PDGFRβ+ (%)
Young
Middle-Aged
b
PDGFRβ Col1a1 DAPI
Col1a1 AUC (x10^7 μm^2)
c
LAMA DAPI
Lama AUC (x 10^7 um^2)
d
PDGFRβ Olig2 DAPI
Olig2+ Counts in PDGFRβ+ Area (mm2)
Middle-aged

Fig 8

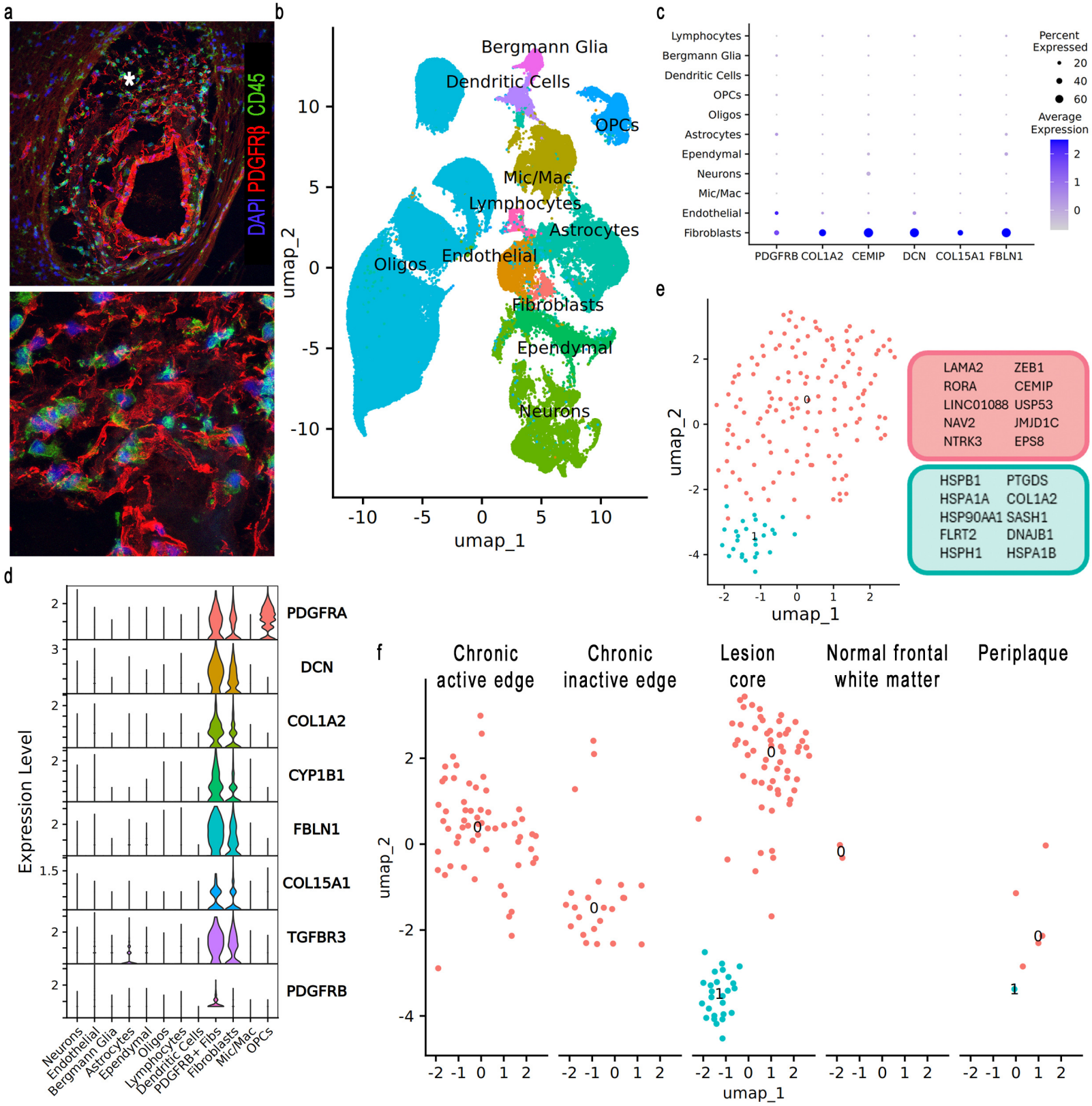
a
DAPI PDGFRβ CD45
b
Bergmann Glia
Dendritic Cells
OPCs
Mic/Mac
Lymphocytes
Astrocytes
Endothelial
Oligos
Fibroblasts
Ependymal
Neurons
umap_1
umap_2
c
Lymphocytes
Bergmann Glia
Dendritic Cells
OPCs
Oligos
Astrocytes
Ependymal
Neurons
Mic/Mac
Endothelial
Fibroblasts
PDGFRB COL1A2 CEMIP DCN COL15A1 FBLN1
Percent Expressed
20
40
60
Average Expression
2
1
0
e
umap_1
umap_2
LAMA2 ZEB1
RORA CEMIP
LINC01088 USP53
NAV2 JMJD1C
NTRK3 EPS8
HSPB1 PTGDS
HSPA1A COL1A2
HSP90AA1 SASH1
FLRT2 DNAJB1
HSPH1 HSPA1B
d
Expression Level
PDGFRA
DCN
COL1A2
CYP1B1
FBLN1
COL15A1
TGFBR3
PDGFRB
Neurons
Endothelial
Bergmann Glia
Astrocytes
Ependymal
Oligos
Lymphocytes
Dendritic Cells
PDGFRB+ Fibs
Fibroblasts
Mic/Mac
OPCs
f
Chronic active edge
Chronic inactive edge
Lesion core
Normal frontal white matter
Periplaque
umap_1
umap_2

Fig 9

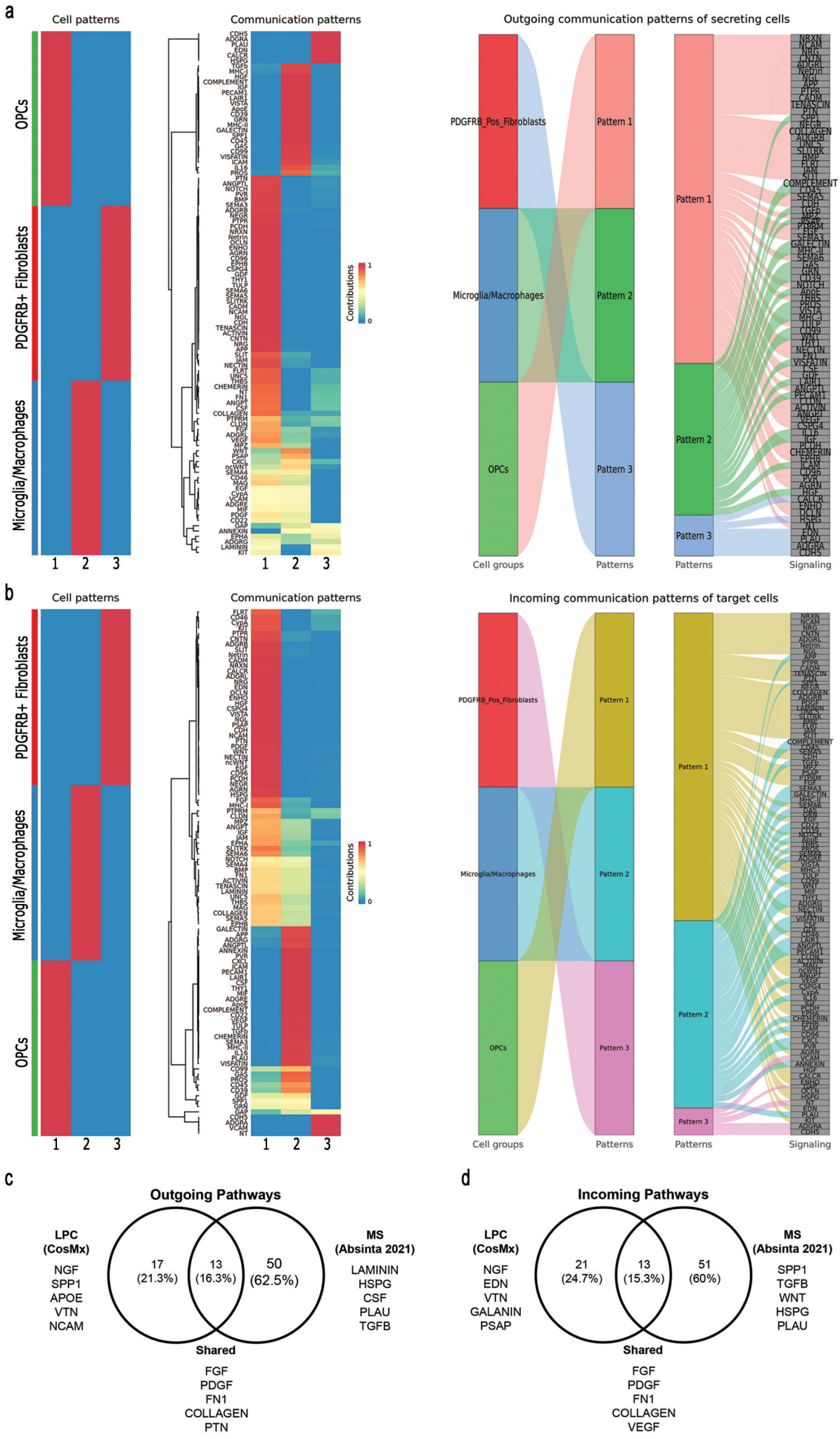
a
Cell patterns
Communication patterns
Outgoing communication patterns of secreting cells
OPCs
PDGFRB+ Fibroblasts
Microglia/Macrophages
Contributions
PDGFRB_Pos_Fibroblasts
Microglia/Macrophages
OPCs
Pattern 1
Pattern 2
Pattern 3
Cell groups
Patterns
Signaling
b
Incoming communication patterns of target cells
c
Outgoing Pathways
LPC (CosMx)
NGF
SPP1
APOE
VTN
NCAM
17 (21.3%)
13 (16.3%)
50 (62.5%)
MS (Absinta 2021)
LAMININ
HSPG
CSF
PLAU
TGFB
Shared
FGF
PDGF
FN1
COLLAGEN
PTN
d
Incoming Pathways
LPC (CosMx)
NGF
EDN
VTN
GALANIN
PSAP
21 (24.7%)
13 (15.3%)
51 (60%)
MS (Absinta 2021)
SPP1
TGFB
WNT
HSPG
PLAU
Shared
FGF
PDGF
FN1
COLLAGEN
VEGF

Fig 10